Journal of Inorganic Biochemistry 163 (2016) 162–175

Contents lists available at ScienceDirect

Journal of Inorganic Biochemistry

journal homepage: www.elsevier.com/locate/jinorgbio

Synthesis, characterization and activity of imidazolate-bridged and Schiff-base dinuclear complexes as models of Cu,Zn-SOD. A comparative study

Verónica A. Daier [a], Eric Rivière [b], Sonia Mallet-Ladeira [c], Diego M. Moreno [a], Christelle Hureau [d,e], Sandra R. Signorella [a,*]

[a] IQUIR (Instituto de Química Rosario), Consejo Nacional de Investigaciones Científicas y Técnicas (CONICET), Facultad de Ciencias Bioquímicas y Farmacéuticas, Universidad Nacional de Rosario, Suipacha 531, S2002LRK Rosario, Argentina
[b] Institut de Chimie Moléculaire et des Matériaux d'Orsay, CNRS, Université Paris Sud, Université Paris Saclay, 91405 Orsay Cedex, France
[c] Institut de Chimie de Toulouse, FR 2599, 118 Route de Narbonne, F-31062 Toulouse, France
[d] CNRS, LCC (Laboratoire de Chimie de Coordination), 205 route de Narbonne, F-31077 Toulouse, France
[e] UPS, INPT, LCC, Université de Toulouse, 205 route de Narbonne, F-31077 Toulouse, France

ARTICLE INFO

Article history:
Received 20 March 2016
Received in revised form 11 June 2016
Accepted 7 July 2016
Available online 9 July 2016

Keywords:
Cu/Zn complexes
SOD activity
Structure
Stability

ABSTRACT

Two imidazolate-bridged diCu^{II} and Cu^{II}Zn^{II} complexes, $[CuZn(dien)_2(\mu\text{-Im})](ClO_4)_3\cdot MeOH$ (**1**) and $[Cu_2(dien)_2(\mu\text{-Im})](ClO_4)_3$ (**2**) (Im = imidazole, dien = diethylenetriamine), and two complexes formed with Schiff base ligands, $[CuZn(salpn)Cl_2]$ (**3**) and $[Cu_2(salbutO)ClO_4]$ (**4**) (H_2salpn = 1,3-bis(salicylidenamino) propane, H_3salbutO = 1,4-bis(salicylidenamino)butan-2-ol) have been prepared and characterized. The reaction of $[Cu(dien)(ImH)](ClO_4)_2$ with $[Zn(dien)(H_2O)](ClO_4)_2$ at pH ≥ 11 yields complex **1**; at lower pH, the Cu_3Zn tetranuclear complex $[\{(dien)Cu(\mu\text{-Im})\}_3Zn(OH_2)(ClO_4)_2](ClO_4)_3$ (**1a**) forms as the main reaction product. X-ray diffraction of **1a** reveals that the complex contains a metal centered windmill-shaped cation having three blades with a central Zn ion and three peripheral capping Cu(dien) moieties bound to the central Zn ion through three imidazolate bridges. The four complexes are able to disproportionate $O_2^{\bullet-}$ in aqueous medium at pH 7.8, with relative rates **4** > **1** > **2** ≫ **3**. $[Cu_2(salbutO)]^+$ (**4**) is the most easily reducible of the four complexes and exhibits the highest activity among the SOD models reported so far; a fact related to the ligand flexibility to accommodate the copper ion in both Cu^{I} and Cu^{II} oxidation states and the lability of the fourth coordination position of copper facilitating stereochemical rearrangements.

1. Introduction

Oxidative stress is caused by an imbalance between the production of reactive oxygen species and the capacity of a biological system for fast removal of these intermediates to prevent cell damage [1,2]. High levels of superoxide are associated to several pathologies like diabetes, numerous neurodegenerative disorders such Alzheimer's and Parkinson's diseases [3–6] and some types of cancer originating from DNA mutations induced by superoxide [7].

The main defence against superoxide radical is a class of enzymes called superoxide dismutases (SODs). There are four types of SODs which differ in the metal center in the active site, the dinuclear Cu,Zn-SOD, and the mononuclear Fe-, Mn- and Ni-SODs. Cu,Zn-SOD is found in all eukaryotic species as a homo-dimeric enzyme of ~32 kDa containing one Cu and one Zn ion per subunit [1,8]. In the dinuclear metal-binding site of the oxidized form of the enzyme, the Cu and Zn ions are bridged by an imidazolate ring from one histidine residue of the protein backbone [9]. In addition to the bridging histidine, the Cu^{II} ion also binds three histidine residues and one water molecule to form a distorted square pyramidal geometry, while the Zn^{II} coordination sphere is completed by two histidine and one aspartate residues in a distorted tetrahedral geometry [10]. Copper is the redox active metal, changing between 2+/1+ oxidation states during catalysis, and zinc plays a role in overall enzyme stability and in facilitating a large pH independence in activity [8].

Because of the limitations associated with the therapeutic applications of the enzyme, such as solution instability, limited cellular accessibility, immunogenicity, bell-shaped dose response curves, short half-lives, costs of production, and proteolytic digestion, a significant amount of research focuses on SOD mimics with low molecular weight aiming at developing potential therapeutic antioxidant compounds [11,12]. A number of Cu^{II} complexes have been characterized as models of the Cu,Zn-SOD enzyme, including Cu^{II} complexes obtained with Schiff base ligands [13–17], imidazolate bridged diCu^{II} [18–22] and heterodinuclear Cu^{II}Zn^{II} complexes [20,23–27]. Although some of

* Corresponding author.
E-mail address: signorella@iquir-conicet.gov.ar (S.R. Signorella).

http://dx.doi.org/10.1016/j.jinorgbio.2016.07.008
0162-0134/

them have proven to be effective in removing superoxide, the key features (type of ligands, nuclearity, redox potential) behind their activity are still elusive. In order to conceive the structural and electronic factors responsible for their ability to disproportionate superoxide, it is important to obtain reliable and comparable values for their SOD activities. The self-decomposition of superoxide to hydrogen peroxide and oxygen in aqueous media ($k = 1 \times 10^5$ M^{-1} s^{-1} to 8×10^5 M^{-1} s^{-1} in the range of pH = 8.1 to 7.1 [28]) is in itself a fast process. Different methods are used for the determination of the rate constant for the superoxide dismutation. Indirect methods (different variations of cytochrome-*c* or NBT assays [29]) that follow the inhibition of the reaction between an indicator and in situ generated superoxide by putative SOD mimics, are spread in the scientific literature. Due to the utilization of different methods and experimental conditions (different superoxide and/or indicator concentrations, buffers and pH values) it is difficult to compare SOD activities reported for SOD mimics. In a number of cases, the IC_{50} values (the [mimic] required for 50% inhibition of the reaction between the indicator and superoxide) are directly compared with reported values, even when different indicators and concentrations were used. Therefore, in this paper we study the SOD activity of two imidazolate-bridged $diCu^{II}$ and $Cu^{II}Zn^{II}$ complexes, $[CuZn(dien)_2(\mu\text{-Im})](ClO_4)_3 \cdot MeOH$ (**1**) and $[Cu_2(dien)_2(\mu\text{-Im})](ClO_4)_3$ (**2**) (dien = diethylenetriamine), and two complexes formed with Schiff base ligands, $[CuZn(salpn)Cl_2]$ (**3**) and $[Cu_2(salbutO)ClO_4]$ (**4**) (H_2salpn = 1,3-bis(salicylidenamino)propane, H_3salbutO = 1,4-bis(salicylidenamino)butan-2-ol), (See Scheme 1)under the very same experimental conditions, and compare their rate constants, k_{McF} – McCord–Fridovich's constant, independent of the type and concentration of the indicator and more appropriate for comparisons [30,31], with other reported Cu,Zn-SOD mimics. The present study adds support to the proposal that the SOD activity mainly depends on the coordination number and geometry of the copper site.

2. Experimental section

2.1. Materials

All reagents were analytical grade chemicals and were used as purchased. Solvents were purified by standard methods.

2.2. Physical measurements

Electronic spectra were recorded on a JASCO V550 spectrophotometer with thermostated cell compartments. IR spectra were recorded on a Perkin-Elmer Spectrum One FT-IR spectrophotometer. The metal content was measured by atomic absorption on a METROLAB 250 AA spectrophotometer. Conductivity measurements were performed using a Horiba F-54 BW conductivity meter on 1.0 mM solutions of the complex in water. ESI-mass spectra were recorded on a Perkin-Elmer SCIEX 365 LCMSMS mass spectrometer. The electrospray solutions were prepared from DMSO solutions of the complexes and diluted with methanol to a $\approx 10^{-5}$ M concentration at a flow rate of 5 μL min^{-1}. EPR data were recorded using an Elexsys E 500 Bruker spectrometer, operating at a microwave frequency of approximately 9.5 GHz. Variable-temperature magnetic susceptibility data were obtained with a Quantum Design MPMS SQUID susceptometer. Diamagnetic corrections were applied by using Pascal's constants. Cu and Zn K-edge XANES (X-ray absorption near edge structure) spectra were recorded at the BM30B (FAME) beamline of the European Synchrotron Radiation Facility (ESRF, Grenoble, France) [32]. The beam energy was selected using an Si(220) N_2 cryo-cooled double-crystal monochromator with an experimental resolution close to that theoretically predicted (namely ~0.5 eV) [33]. The beam spot on the sample was approximately 300 × 200 μm^2 (H × V, FWHM). Spectra were recorded in absorption mode with a 30-element solid state Ge detector (Canberra) in liquid cells in a He cryostat. The temperature was kept at 10 K during data collection to prevent sample damage and the absence of significant photo-reduction of the Cu^{II} samples was checked. The energy was calibrated with Cu and Zn metallic foils, such that the maximum of the first derivative was set at 8979 and 9659 eV, respectively. Cu data were collected from 8840 to 8960 eV using a 5 eV step of 2 s, from 8960 to 9020 eV using a 0.5 eV step of 3 s, and from 9020 to 9300 eV with a k-step of 0.05 $Å^{-1}$ and an increasing time of 2–10 s per step. Zn data were collected from 9510 to 9630 eV using a 5 eV step of 2 s, from 9630 to 9700 eV using a 0.5 eV step of 3 s, and from 9700 to 10,000 eV with a k-step of 0.05 $Å^{-1}$ and an increasing time of 2–10 s per step. XANES spectra were background-corrected by a linear regression through the pre-edge region and a polynomial through the post-edge region and normalized to the edge jump. XANES samples were prepared in a BN

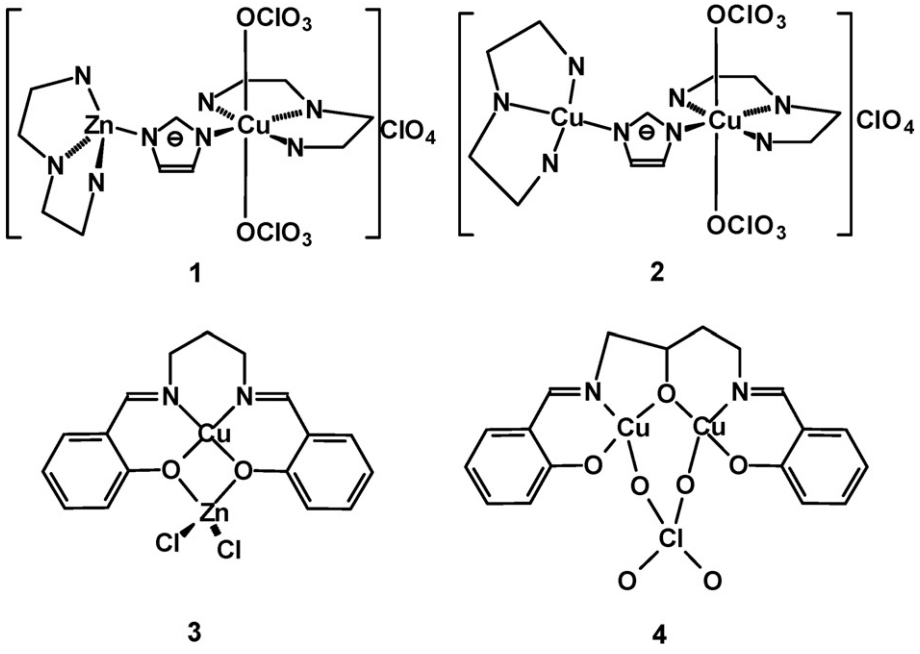

Scheme 1. Dinuclear complexes studied in this work.

matrix. Electrochemical studies of complexes were performed with a computer-controlled Princeton Applied Research potentiostat, model VERSASTAT II, with model 270/250 Research Electrochemistry Software. The cyclic voltammetry experiments were done using a conventional three electrode system under argon atmosphere in degassed DMF solutions containing 0.1 M Bu_4NPF_6 as supporting electrolyte and 10^{-3} M of the complex. Pt electrodes were used as working and counter electrodes and Ag/AgCl as reference electrode. The electrochemical system was calibrated with a ferrocene/ferrocenium redox system ($E_{1/2}$ = 481 mV).

2.3. Calculations

Geometry optimizations were performed using the Gaussian 09 program [34]. Calculations were done at Density Functional Theory (DFT) level, applying the B3LYP functional and 6-31G** basis set on all atoms [35,36].

2.4. Synthesis of complexes

2.4.1. [CuZn(dien)$_2$(μ-Im)](ClO$_4$)$_3$·MeOH (**1**) and [{(dien)Cu(μ-Im)}$_3$Zn(H$_2$O)(ClO$_4$)$_2$](ClO$_4$)$_3$ (**1a**)

Complex **1** was obtained by a described procedure, that consists in mixing equimolar 5:1 methanol:acetonitrile solutions of [Cu(dien)ImH](ClO$_4$)$_2$ and [Zn(dien)(H$_2$O)](ClO$_4$)$_2$, followed by addition of NaOH 1 M up to pH 12 [37]. Yield: 59% (2.16 g, 2.95 mmol). Anal. Calc. for $CuZnC_{12}Cl_3N_8H_{33}O_{13}$: C 19.86, Cu 8.68, H 4.03, N 15.45, Zn 8.81%; found: C 19.84, Cu 9.15, H 4.39, N 15.32, Zn 9.09%. Significant IR bands (KBr, ν cm^{-1}): ν_{N-H} 3456/3238, ν_{C-H} 2949/2895, $\nu_{C=C,C=N(Im)}$ 1450–1650, ν_{ClO4} 1093/625, $\nu_{Cu/Zn-N}$ 420. UV–visible: λ_{max} nm (ε, M^{-1} cm^{-1}) 605 (105) in DMSO. Molar conductivity (water) = 301 Ω^{-1} cm^2 mol^{-1}. To obtain complex **1a**, Et_3N was used instead of NaOH and pH raised to 9 instead of 12. Cu(ClO$_4$)$_2$·6H$_2$O (1.857 g, 5 mmol) was dissolved in methanol/acetonitrile 5:1 (60 mL) and dien (540 μL, 5 mmol) was added to the solution and stirred for 30 min. Then imidazole (0.340 g, 5 mmol) was added, and the solution turned dark blue. The mixture was left to stir overnight. Dien (540 μL, 5 mmol) was added to a solution of Zn(ClO$_4$)$_2$·6H$_2$O (1.920 g, 5 mmol) in methanol/acetonitrile 1:5 (60 mL) and the mixture stirred overnight. The solutions of [Cu(dien)(ImH)](ClO$_4$)$_2$ and [Zn(dien)(H$_2$O)](ClO$_4$)$_2$ were mixed and the pH adjusted to 9 with Et_3N. The resulting solution was left to react overnight at room temperature. The volume was reduced to one half and a white solid was filtered out (containing 16% of initial Zn). After 2 h, **1**(ClO$_4$)$_3$ precipitated from the filtrate as a dark blue solid (6.6%). Upon standing in air for several days, blue crystals were collected from the filtrate of the reaction mixture to give complex [{(dien)Cu(μ-Im)}$_3$Zn(H$_2$O)(ClO$_4$)$_2$](ClO$_4$)$_3$ (**1a**) (1.47 g, 1.15 mmol). These crystals were suitable for X-ray diffraction.

2.4.2. [Cu$_2$(dien)$_2$(μ-Im)](ClO$_4$)$_3$ (**2**)

This compound was prepared through a synthetic procedure slightly modified from that published for a related complex [38]. Dien (1.08 μL, 5 mmol) was added to a solution of Cu(ClO$_4$)$_2$·6H$_2$O (3.7053 g, 10 mmol) in methanol/acetonitrile 5:1 (250 mL) and stirred for 30 min. Then imidazole (0.340 g, 5 mmol) was added and the solution turns dark blue immediately. The pH value was adjusted to 10 with NaOH. The resulting solution was left to react overnight at room temperature and then the volume was reduced. A dark blue precipitate formed and was collected by filtration. Yield: 58% (2.0187 g, 2.887 mmol). Anal. Calc. for $Cu_2C_{11}Cl_3N_8H_{29}O_{12}$: C 18.91, H 4.18, N 16.03, Cu 18.18%; found: C 18.58, H 4.39, N 15.8, Cu 18.17%. Significant IR bands (KBr, ν cm^{-1}): ν_{N-H} 3261/3344 cm^{-1}, ν_{Im} 1450–1650, ν_{ClO4} 1100/624, ν_{Cu-N} 419. UV–visible λ_{max} 593 nm (ε = 223 M^{-1} cm^{-1}) in DMF. Molar conductivity (water) = 340 Ω^{-1} cm^2 mol^{-1}.

2.4.3. [CuZn(salpn)Cl$_2$] (**3**)

A solution of H_2Salpn (0.263 g, 1 mmol) in DMF (5 mL) was added to a mixture of Cu(ClO$_4$)$_2$·6H$_2$O (0.546 g, 1.5 mmol) and $ZnCl_2$ (1.125 g, 1 mmol) in DMF (12 mL). The green solution was stirred for 30 min at 47 °C. MeOH (12 mL) was added and the solution kept at −4 °C until a green solid separated. The solid was collected by filtration, washed twice with cold methanol and dried under vacuum. Yield: 50% (0.230 g, 0.5 mmol), Anal. Calc. for $CuZnC_{17}Cl_2H_{16}N_2O_2$: C 42.52, H 3.55, N 5.83, Cu 13.23, Zn 13.61%. Found: C 42.5, H 3.29, N 5.66, Cu 15.81, Zn 13.56%. Significant IR bands (KBr ν cm^{-1}): $\nu_{C=N}$ 1623, ν_{Ar-O} 1218, $\nu_{Cu-N/O}$ 475, 455. UV–visible: λ_{max} 613 nm (ε = 169 M^{-1} cm^{-1}) in DMSO. Single crystals of **3** suitable for X-ray diffraction were obtained from the filtrate of the reaction mixture upon standing in air for several days.

2.4.4. [Cu$_2$(SalbutO)(ClO$_4$)] (**4**)

A solution of H_3salbutO [39] (0.128 g, 0.408 mmol) in 10 mL of MeOH was added dropwise to a mixture of Cu(ClO$_4$)$_2$·6H$_2$O (0.306 g 0.825 mmol) and imidazol (0.028 g, 0.413 mmol) in MeOH (25 mL). The pH of the mixture was raised to 11 upon addition of KOH in methanol/H_2O. The green solution was stirred for 24 h at 25 °C. A green solid was collected by filtration and washed twice with cold methanol and water. Recrystallization from cold DMF afforded a dark green polycrystalline solid of **4**. Yield: 24% (0.052 g, 0.097 mmol). Anal. Calc. for $Cu_2C_{18}ClH_{17}N_2O_7$: C 40.34, H 3.19, N 5.22, Cu 23.71%. Found: C 39.42, H 2.92, N 5.17, Cu 24.91%. Significant IR bands (KBr ν cm^{-1}): $\nu_{C=N}$ 1630, ν_{Ar-O} 1278, ν_{ClO4} 1214/1098/1035, $\nu_{Cu-N/O}$ 467. UV–visible λ_{max} nm (ε, M^{-1} cm^{-1}) 620 (268), 385 (4100), 270 (20,850) in DMSO.

2.4.5. Caution

Although we have experienced no difficulties with the perchlorate salts they should nevertheless be regarded as hazardous and treated with care.

2.5. Indirect SOD assay

The SOD activity of the complexes was assayed by measuring inhibition of the photoreduction of nitro blue tetrazolium (NBT), by a method slightly modified from that originally described by Beauchamps and Fridovich [40]. The reaction of methionine and rivoflavine, in the presence of light, is the source of superoxide. This assay is based on kinetic competition for the superoxide reaction between NBT and the complex with SOD activity. In this way the SOD activity is inversely related to the amount of formazan, the purple product formed by a reaction of NBT with superoxide, observed at 560 nm. The solutions were prepared with 0.05 M phosphate buffer of pH 7.8, riboflavin (3.4×10^{-6} M), methionine (0.01 M), NBT (4.6×10^{-5} M) and a complex of different concentrations. Riboflavin was last added and the reaction was initiated by illumination of the mixtures with a fluorescent lamp of constant light intensity at 25 °C. The reduction of NBT was monitored at 560 nm after an illumination period of 15 min. The IC_{50} values (the concentration of the SOD mimic that induces a 50% inhibition of the reduction of NBT) were determined from concentration-dependent plots. Control reactions confirm that the compounds did not directly react with NBT or riboflavin. Inhibition percentage was calculated according to: $\{(\Delta Abs / t)_{without\ complex} - (\Delta Abs / t)_{with\ complex}\} \times 100 / (\Delta Abs / t)_{without\ complex}$.

2.6. Crystallographic data collection and structure determination

Crystallographic data for compounds [(dienCuIm)$_3$Zn(H$_2$O)(ClO$_4$)$_2$](ClO$_4$)$_3$ (**1a**) and [Cu(salpn)ZnCl$_2$] (**3**) were collected at 180(2) K on an Bruker Kappa APEX II Diffractometer, using graphite-monochromated Mo-Kα radiation (λ = 0.71073 Å) and equipped with an Oxford Cryosystems Cryostream cooler device. Unit cell determination, data collection, and reduction were carried out using the Bruker APEX2 package and associated integration program SAINT [41].

The structure was solved by direct methods with SHELXS-97 and refined by full-matrix least-squares on F^2 data with SHELXL-97 [42] using anisotropic displacement parameters for non-hydrogen atoms. Molecular plots were drawn using the ORTEP program [43], with 50% probability displacement ellipsoids, and the packing diagrams were generated with CAMERON [44]. Crystal data collection and refinement parameters are summarized in Table 1.

3. Results and discussion

3.1. Preparation and characterization of complexes *1–4*

Several procedures have been proposed to obtain imidazolate-bridged Cu,Zn complexes with capping polyamines. In some cases, a direct mixture of Cu and Zn salts + alkaline imidazol + capping ligand was used [20], and in most cases the method of choice consisted in mixing equimolar $[Cu(L)(ImH)]^{2+}$ and $[Zn(L)(H_2O)]^{2+}$ solutions followed by addition of NaOH up to pH ~ 12 [45–47]. In these reactions, pH control is a critical point. Thus, the mixture of $[Cu(dien)(ImH)](ClO_4)_2$ and $[Zn(dien)(H_2O)](ClO_4)_2$ at pH 11–12 yields complex **1** as the main reaction product [37] but, at lower pH, the reaction products' distribution is very different. When pH is adjusted to 9, compound **1** is obtained as a minor product from a reaction mixture of $[Cu(dien)(ImH)](ClO_4)_2$ and $[Zn(dien)(H_2O)](ClO_4)_2$ in methanol/acetonitrile, the main species being the Cu_3Zn tetranuclear complex **1a**. After filtration of the heterodinuclear complex **1**, crystals of $[\{(dien)Cu(\mu\text{-}Im)\}_3Zn(OH_2)(ClO_4)_2](ClO_4)_3$ (**1a**) separated from the solution, which were analyzed by X-ray diffraction. This compound crystallizes in the $P2_1/n$ space group with the asymmetric unit containing a tetranuclear complex cation, two coordinated perchlorate and three non-coordinating perchlorate anions. The molecular structure of **1a** is illustrated in Fig. 1 and consists of a metal centered windmill-shaped cation having three blades with a central Zn ion and three peripheral capping Cu(dien) moieties bound to the central Zn ion through three imidazolate bridges. Relevant bond distances and angles of complex **1a** are summarized in Table 2. The coordination polyhedron around Cu(2) is an elongated rhombic octahedron in which the equatorial plane is defined by the N_4 donor set from dien and Im^- ligands, and the apical positions are occupied by two oxygen atoms of one terminal monodentate (O(18)-ClO_3^-) and one bridging tridentate (O(8)-ClO_3^-) perchlorate anions, the last shared by Cu(1), Cu(2) and Cu(3) of three adjacent molecules, with Cu—O distances 2.650(5), 2.747(5) and 2.579(10) Å, respectively. The terminal ClO_4^- binds to Cu(2) with a Cu—O length of 2.682(10) Å. Cu(1) and Cu(3) atoms are penta-coordinated and assume a square-pyramidal configuration with four nitrogen atoms from dien and Im^- occupying the basal plane and one oxygen of the tridentate perchlorate (O(6)/O(9)-ClO_3^-) at the apex. For the three Cu centers, the ranges of *cis* and *trans* N—Cu—N angles are 83.41(14)–97.02(13)° and 165.16(13)–179.27(14)°, respectively (Table 2), while the O—Cu—N angles lie in the range of 88.1(2)–97.1(2)° (Cu(3)), 81.1(1)–99.4(1)° (Cu(2)) and 80.9(1)–106(9)1° (Cu(1)), evidencing rhombic distortion. The displacements of the Cu ion from the least-squares N_4 equatorial plane are 0.109(2), 0.059(2) and 0.071(2) Å, for Cu(1), Cu(2) and Cu(3), respectively. The Zn atom is tetra-coordinated to three imidazolate and one H_2O molecule. The geometry around the central metal ion is distorted-tetrahedral, with N—Zn—N angles (103.80(12)–119.24(13)°) more deviated than N—Zn—O angles (101.90(15)–114.23(14)°) with respect to the ideal value. The distance between the central Zn and peripheral Cu in **1a** lies in the range 5.863(1)–5.999(1) Å, which is similar to that observed in dinuclear imidazolato-bridged Cu,Zn systems, such as $[(tren)Cu(\mu\text{-}Im)Zn(tren)](ClO_4)_3$ (5.84 Å) [48], $[(trien)Cu(\mu\text{-}Im)Zn(trien)](ClO_4)_3$ (6.081 Å) [45], $[(dtma)Cu(\mu\text{-}Im)Zn(dtma)]ClO_4$ (6.0 Å) [46] and $[(Cu(\mu\text{-}Im)ZnL_{-2H})(Cu(\mu\text{-}Im)ZnL_{-H})](ClO_4)_3$ (5.95 Å, L = macrocycle) [25]. To our knowledge, this type of windmill-shaped $ZnCu_3$ system had not been observed previously. The other reported $ZnCu_3$ complex is a star-shaped molecule formed with a Schiff-base ligand where the central···peripheral metal ions are linked through two phenolato bridges, resulting in short Zn···Cu distances that are in the range of 3.05–3.10 Å [49].

Fig. 2 displays the crystal packing of compound **1a** along a-axis. In the crystal structure, each tetranuclear entity is connected to six adjacent $ZnCu_3$ complex cations through the coordination of Cu(2), Cu(3), and O(6) and O(9) of the perchlorato groups of the basic tetranuclear unit to the respective O(8), O(9), Cu(1) and Cu(3) from adjacent complex cations, forming 2-D polymeric layers with non-coordinating ClO_4^- ions intercalated among them.

Crystals suitable for X-ray diffraction studies could not be obtained for the dinuclear complex **1**, but the Zn content and XANES spectra (see below) confirm that the heterodinuclear complex formed in the solid state. X-band EPR spectra of the complex recorded on

Table 1
Summary of crystal data for complexes **1a** and **3**.

Empirical formula	$C_{21}H_{50}CU_3N_{15}O_1ZN$, $5(CLO_4)$	$C_{17}H_{16}CL_2CUN_2O_2ZN$
M	1282.05	480.16
T	180(2) K	180(2) K
Wavelength	0.71073 Å	0.71073 Å
Cryst syst, space group	Monoclinic, $P2_1/N$	Monoclinic, $P2_1/C$
Unit cell dimensions	a = 12.8237(5) Å	a = 11.5722(4) Å
	b = 16.5024(8) Å	b = 8.1677(3) Å
	c = 21.5806(10) Å	c = 18.2906(7) Å
	α, γ = 90°, β = 90.141(2)°	α, γ = 90°, β = 99.132(2) °
V	4566.9(4) $Å^3$	1706.88(11) $Å^3$
Z, ρ_{CALCD}	4, 1.865 Mg/m^3	4, 1.868 Mg/m^3
μ_{MO}	2.281 mm^{-1}	2.978 mm^{-1}
F(000)	2604	964
Cryst size	0.12 × 0.10 × 0.08 mm	0.16 × 0.12 × 0.08 mm
θ range for data collection	5.13 to 26.37°	2.64 to 25.38°
Limiting indices	$-16 \le h \le 16$, $-20 \le k \le 20$, $-26 \le l \le 26$	$-12 \le h \le 13$, $-9 \le k \le 9$, $-18 \le l \le 22$
Reflns collected/unique	55,969/55,969 [R(INT) = 0.0792]	19,809/3100 [R(INT) = 0.0353]
Completeness to θ = 25.35	99.1%	99.2%
Max and min transmission	0.8386 and 0.7715	0.7966 and 0.6473
Refinement method	Full-matrix least-squares on F^2	Full-matrix least-squares on F^2
Data/restraints/parameters	55,969/336/710	3100/0/226
Goodness-of-fit on F^2	1.031	1.032
Final R indices [$I > 2\sigma(I)$]	$R_1 = 0.0626$, $wR_2 = 0.1311$	$R_1 = 0.0233$, $wR_2 = 0.0487$
R indices (all data)	$R_1 = 0.0994$, $wR_2 = 0.1519$	$R_1 = 0.0335$, $wR_2 = 0.0523$
Largest diff. peak and hole	1.244 and −0.900 E $Å^{-3}$	0.311 and −0.293 e $Å^{-3}$

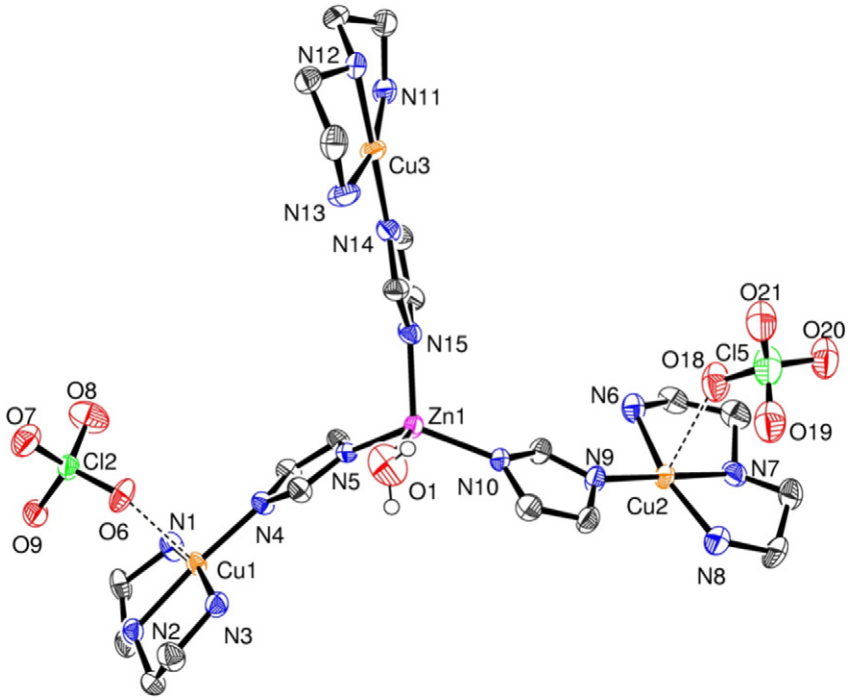

Fig. 1. ORTEP drawing of $[\{(dien)Cu(\mu\text{-}Im)\}_3Zn(OH_2)(ClO_4)_2]^{3+}$ (**1a**$^{3+}$). Hydrogen atoms and non-coordinated perchlorate anions are omitted for clarity.

polycrystalline samples (Fig. 3) show axial features at room and liquid nitrogen temperature with *g*-tensor values $g_{//} = 2.2$ and $g_{\perp} = 2.054$, which evidence that the Cu^{II} ion is in nearly square-planar geometry such as in **1a**.

Complex $[Cu_2(dien)_2(\mu\text{-}Im)](ClO_4)_3$ (**2**) was obtained by reacting the Cu^{2+} salt + dien + ImH (2:1:1 ratio) in CH_3CN/CH_3OH of pH 10. The same product is obtained with a similar yield from a mixture of equimolar $[Cu(dien)ImH](ClO_4)_2$ and $[Cu(dien)(H_2O)](ClO_4)_2$ solutions at pH 11 [50,51]. When lowering the pH to 9, the reaction yield keeps constant. Thus, at pH ≥ 9 this reaction afford **2** as the major product, while for the Cu,Zn analogue, **1**, the pH must be ≥11.

In order to determine the degree of interaction between the two unpaired electrons of **2** through the bridging imidazolate ligand, magnetic susceptibility (χ_M) was measured under a 1000 Oe field in the 2–300 K temperature range on a powdered sample. As shown in Fig. 4, when the temperature decreases, χ_M increases continuously, reaches a maximum around 60 K, and then falls to a minimum at 14 K. This behavior,

Table 2
Selected bond lengths (Å) and angles (°) for **1a**.

Cu(1)-N(1)	2.005(3)	Cu(2)-O(18)	2.682(10)
Cu(1)-N(2)	2.008(3)	Cu(3)-N(11)	2.028(3)
Cu(1)-N(3)	2.005(3)	Cu(3)-N(12)	2.014(3)
Cu(1)-N(4)	1.951(3)	Cu(3)-N(13)	2.038(3)
Cu(1)-O(6)	2.650(5)	Cu(3)-N(14)	1.951(3)
Cu(2)-N(6)	2.008(3)	Cu(3)-O(9)	2.579(10)
Cu(2)-N(7)	2.005(3)	Zn(1)-N(5)	1.980(3)
Cu(2)-N(8)	2.020(3)	Zn(1)-N(10)	1.977(3)
Cu(2)-N(9)	1.956(3)	Zn(1)-N(15)	1.983(3)
Cu(2)-O(8)	2.745(5)	Zn(1)-O(1)	2.056(4)
N(4)-Cu(1)-N(3)	95.32(12)	N(10)-Zn(1)-N(5)	119.24(13)
N(4)-Cu(1)-N(1)	96.52(12)	N(10)-Zn(1)-N(15)	113.26(13)
N(3)-Cu(1)-N(1)	165.48(12)	N(5)-Zn(1)-N(15)	103.80(12)
N(4)-Cu(1)-N(2)	175.27(14)	N(10)-Zn(1)-O(1)	101.90(15)
N(3)-Cu(1)-N(2)	83.79(12)	N(5)-Zn(1)-O(1)	104.51(13)
N(1)-Cu(1)-N(2)	83.72(12)	N(15)-Zn(1)-O(1)	114.23(14)
N(9)-Cu(2)-N(7)	179.19(15)	N(14)-Cu(3)-N(12)	179.27(14)
N(9)-Cu(2)-N(6)	97.02(13)	N(14)-Cu(3)-N(11)	96.74(13)
N(7)-Cu(2)-N(6)	83.53(15)	N(12)-Cu(3)-N(11)	83.83(13)
N(9)-Cu(2)-N(8)	95.05(14)	N(14)-Cu(3)-N(13)	95.97(14)
N(7)-Cu(2)-N(8)	84.34(15)	N(12)-Cu(3)-N(13)	83.41(14)
N(6)-Cu(2)-N(8)	166.40(14)	N(11)-Cu(3)-N(13)	165.16(13)
O(8)-Cu(2)-O(18)	170.8(2)		

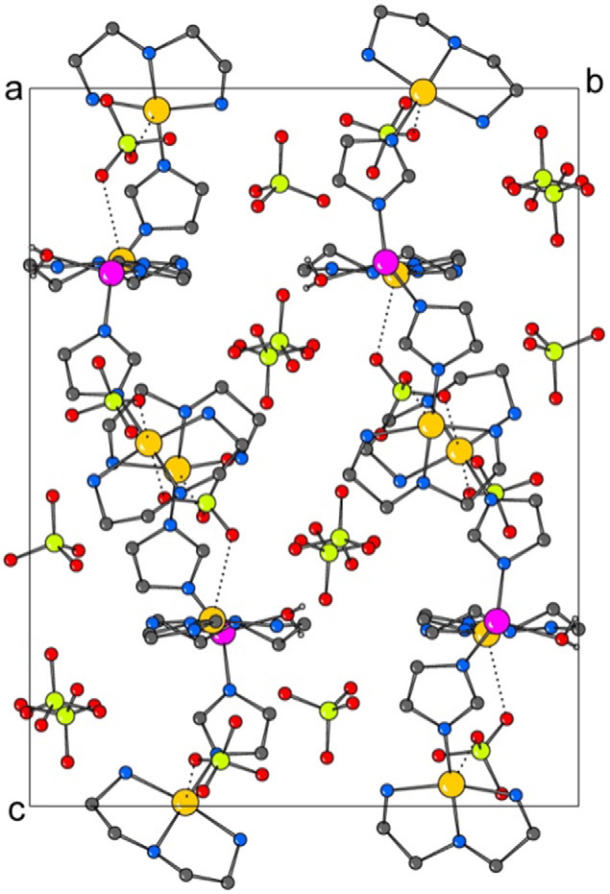

Fig. 2. Packing diagram of **1a** viewed along the crystallographic a-axis.

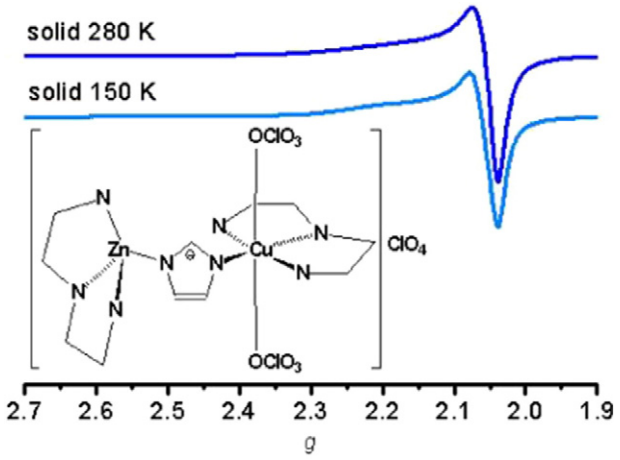

Fig. 3. X-band EPR spectra of polycrystalline **1**.

together with the monotonic decreasing of the $\chi_M T$ product upon cooling, from 0.74 at 300 K to 0 cm^3 K mol^{-1} at 13 K, is typical of antiferromagnetic exchange interaction between two Cu^{II} ions. The rise of χ_M below 13 K is due to small amounts of monomeric Cu^{2+} paramagnetic impurities.

The temperature dependence of the χ_M data were fitted to the Bleaney–Bowers equation for exchange-coupled pairs of Cu^{II} ions corrected for a paramagnetic monomeric Cu^{2+} impurity (Eq. (1)) [52]. In this equation, J represents the magnetic exchange parameter, g is the Landé factor and p is the molar fraction of paramagnetic impurity. The best fit (solid line in Fig. 4) of the χ_M vs T and $\chi_M T$ vs T data leads to the following parameters: $J = -68.9\ cm^{-1}$, $g = 2.09$, $p = 1.3 \times 10^{-2}$, $R\chi = 7.9 \times 10^{-6}$ and $R\chi_T = 1.0 \times 10^{-5}$ where $R\chi_T = \sum(\chi_{cal}T - \chi_{exp}T)^2 / \sum(\chi_{exp}T)^2$ and $R\chi = \sum(\chi_{cal} - \chi_{exp})^2 / \sum(\chi_{exp})^2]$.

$$\chi_M = (1-p)2Ng^2\beta^2[kT(3 + \exp(-J/kT))]^{-1} + pNg^2\beta^2/2kT \quad (1)$$

The magnitude of J has been shown to depend particularly on the angle ϕ of the Cu—N(Im)—(Im) bonds and on the dihedral angle α between the imidazolate ring and the copper coordination plane. The ϕ values are important in determining the value of J for a σ pathway, so as the increase in these angles would produce stronger coupling ($|J|$ is

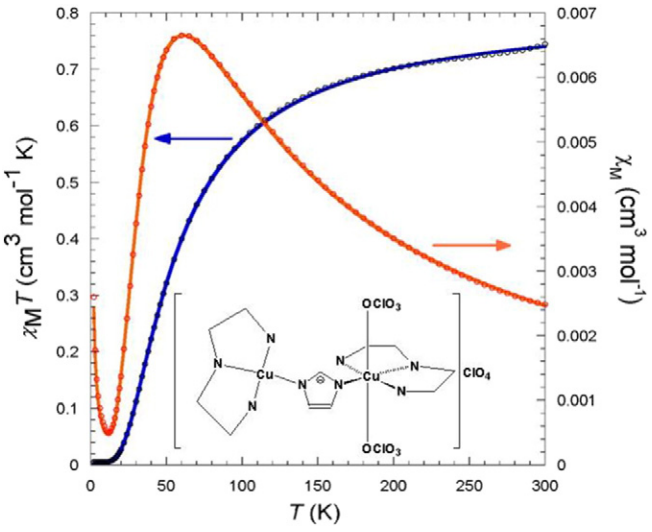

Fig. 4. Temperature dependence of χ_M and $\chi_M T$ for compound **2**: (O) experimental data, solid lines show the simulation obtained with Eq. (1).

maximum for $\phi = 144°$). Besides, when dihedral angles α are considerably different from 0 or 90° π interactions are favored. A crystal structure had been reported for **2** [51]. From the structural data, the Cu···Cu distance is 5.82 Å, the ϕ values are 123 and 124°, and the α dihedral angles are approximately 45.4 and 19.7° by considering a square pyramidal geometry with the N_4 set as the basal plane for each Cu ion. These values of α would favor a π exchange pathway in **2** leading to an antiferromagnetic interaction higher than for imidazolate-bridged Cu_2 complexes in which the σ exchange pathway predominate [22], but close to those found for other $Cu^{II}(\mu$-Im)Cu^{II} complexes with similar geometry [18,53].

Complex [Cu(salpn)$ZnCl_2$] (**3**) was obtained from a mixture of salpn, $Cu(ClO_4)_2$ and $ZnCl_2$ in DMF/MeOH. This compound crystallizes in the $P2_1/c$ space group with the asymmetric unit containing the binuclear Cu,Zn complex molecule shown in Fig. 5(a), together with relevant bond lengths and angles. The Cu ion is located in a slightly distorted square-planar coordination polyhedron defined by the N_2O_2 donor set from salpn. The Zn atom is tetra-coordinated to two *O*-phenolato from salpn and two chloride anions. The geometry around the Zn ion is distorted-tetrahedral, with the Cl—Zn—Cl plane nearly perpendicular to the Cusalpn unit. In each molecule, Cu, Zn and the two *O*-phenolato define a CuO_2Zn unit with angles Cu—O—Zn 102.45(7)°, O—Cu—O 77.87(7)° and O—Zn—O 75.12(6)°. The Cu(μ-OPh)$_2$Zn moiety is also almost planar with a dihedral angle between the planes Cu(1)O(1)O(2) and Zn(1)O(1)O(2) equal to 13.86(12)°, resulting in a Cu···Zn distance of 3.0783(4) Å. The same compound had been obtained in a two step procedure – [Cu(salpn)] was first obtained and then reacted with $ZnCl_2$ – from dioxane/methanol, without reporting yield [54] and from methanol, with similar yield [55].

The packing of the dinuclear units in the crystal may result from intermolecular H-bonds and π–π stacking interactions forming a 3D network. As shown in Fig. 5(b) the unit cell ($z = 4$) includes four symmetry-related molecules. Cl(1) of the basic molecule (A) and its congener through an inversion center (B) are connected to molecules D and C, respectively, through weak H-bond (Cl(1)···HC(8) 3.238 Å). A/B molecules interact through π–π stacking, with a centroid-to-centroid distance of 3.573 Å between overlapping aromatic rings. The Cu centers are well distant from each other, separated by 9.533(1) Å (between A/C and B/D molecules) and 9.795(1) Å (between B/C or A/D molecules). Therefore, in the solid state the copper centers are well isolated without spin–spin interactions.

However, in DMSO solution, EPR and mass spectra evidence formation of dimeric species. The EPR spectrum of **3** in frozen DMSO solution is displayed in Fig. 6(a). The spectrum exhibits the typical features for a Cu^{II} in axial symmetry (signal S1) flanked by the $\Delta M_S = \pm 1$ transitions from the triplet state of a spin-coupled Cu^{II} system (signal S2) [56]. The measured spectral parameters for the uncoupled Cu^{II} site (S1) are: $g_\perp = 2.023$, $g_{//} = 2.25$ and $A_{//} = 184 \times 10^{-4}\ cm^{-1}$, and for the spin-coupled system (S2): $g_\perp = 2.056$, $g_{//} = 2.20$ and $A_{//} = 77 \times 10^{-4}\ cm^{-1}$. The hyperfine splitting constant observed on the parallel components of S2 is nearly one half of S1, which supports the assignment. This means that in solution, the $ZnCl_2$ moiety dissociates, at least partially, and [Cu(salpn)] forms the dimer, as already observed for [Cu(salen)] [57] and other Cu–Schiff base complexes [58]. In the solid, the $ZnCl_2$ moiety keeps the copper ions far apart precluding spin–spin interactions.

The formation of the $[Cusalpn]_2$ dimer was confirmed by ESI-mass spectra of **3** in DMSO. As shown in Fig. 6(b), besides the main peak at $m/z = 344.1$ (100%) belonging to $[Cu(salpn)H]^+$ monocation, another major peak appears at $m/z = 687.1$ (86%) with the isotopic pattern of a dimeric species, which can be attributed to the $[(Cusalpn)_2H]^+$ monocation. No Cu,Zn species were observed in the mass spectra, although this can result from dissociation during the electrospray.

The dark green Cu^{II}_2 complex of the N_2O_3 Schiff base ligand H_3salbutO **4** was obtained by mixing the ligand with the Cu^{II} salt in the presence of imidazole in methanol/H_2O at pH 11. Formation of the dinuclear species is clearly related to the flexibility of the ligand,

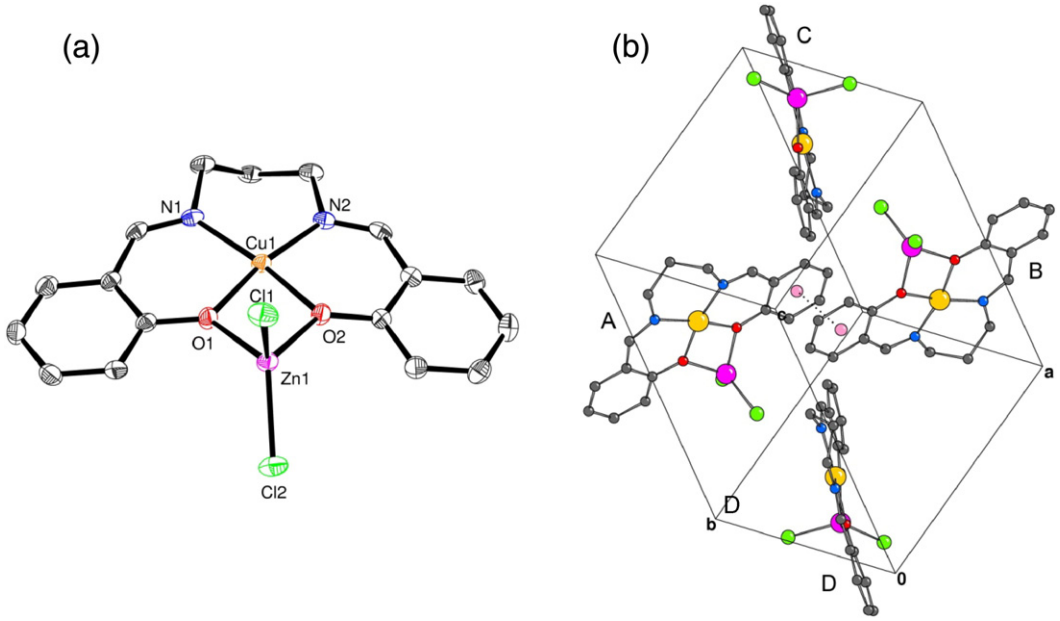

Fig. 5. (a) Plot of the asymmetric unit of [CusalpnZnCl$_2$] (**3**). Hydrogen atoms have been omitted for clarity. Selected bond lengths (Å) and angles (°): N(1)-Cu(1) 1.962(2), N(2)-Cu(1) 1.966(2), O(1)-Cu(1) 1.945(2), O(2)-Cu(1) 1.943(2), O(1)-Zn(1) 2.003(2), O(2)-Zn(1) 2.005(2), Cl(1)-Zn(1) 2.210(1), Cl(2)-Zn(1) 2.212(1), Cu(1)-Zn(1) 3.078(1), O(2)-Cu(1)-O(1) 77.87(7), O(2)-Cu(1)-N(1) 167.94(8), O(1)-Cu(1)-N(1) 91.33(8), O(2)-Cu(1)-N(2) 92.54(7), O(1)-Cu(1)-N(2) 169.95(7), N(1)-Cu(1)-N(2) 98.50(8), O(1)-Zn(1)-O(2) 75.12(6), O(1)-Zn(1)-Cl(1) 108.57(5), O(2)-Zn(1)-Cl(1) 112.36(5), O(1)- Zn(1)-Cl(2) 119.68(5), O(2)-Zn(1)-Cl(2) 118.07(5), Cl(1)-Zn(1)-Cl(2) 116.30(3). (b) Crystal packing diagram of **3** depicting a π–π stacking interaction.

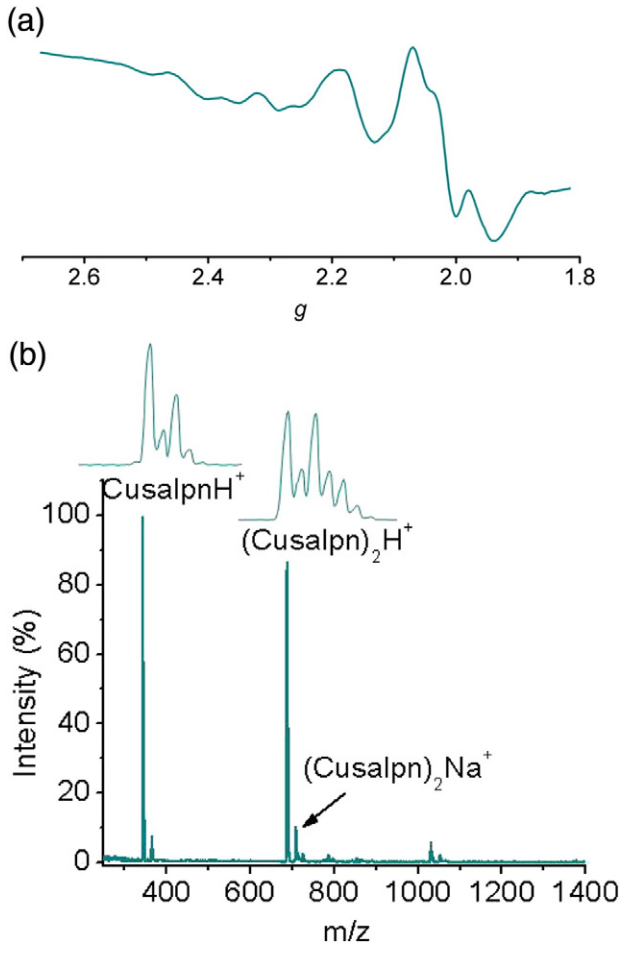

Fig. 6. (a) EPR spectrum of a DMSO frozen solution of **3**. $T = 100$ K. (b) Positive mode ESI-mass spectrum of **3** in DMSO.

which can accommodate the two Cu^{II} ions. However, contrary to the expectation, the dinuclear complex contains ClO_4^- instead of the Im^- ligand. In the solid-state IR spectrum of **4**, instead of the intense single band expected for ionic perchlorate of T_d symmetry at 1100 cm^{-1}, broad peaks are found at 1214, 1098 and 1035 cm^{-1} (Fig. 7(a)) which fall in the ranges assignable to bidentate perchlorate of symmetry C_{2v} [59]. In the solid, perchlorate probably occupies the fourth coordination position of the Cu^{II} ions acting as a bridge between them. An optimized geometry for this complex is shown in Fig. 7(b), together with calculated bond distances and angles. In this structure, the Cu ions are doubly bridged by the central alkoxo group of the Schiff-base ligand and perchlorate, with Cu ions in a tetrahedrically distorted square-planar environment defined by the NO_3 donor set from salbutO^{3-} and ClO_4^-. The calculated Cu···Cu distance (3.436 A°) and Cu—O—Cu bridging angle (126.8°) are in the range found for alkoxo-bridged diCu^{II} compounds [60–64].

Magnetic susceptibility of compound **4** was measured on a powdered sample in the 2–300 K temperature range. The observed $\chi_M T$ value at 300 K was 0.104 cm^3 mol^{-1} K, which is considerably lower than the spin-only value expected for two noninteracting Cu^{II} centers (0.75 cm^3 mol^{-1} K with $g = 2.0$). Upon lowering of the temperature, the $\chi_M T$ value decreases steadily to 0.0039 cm^3 mol^{-1} K at 44 K (below this temperature, there is an increase in magnetic susceptibility due to the presence of a small amount of monomeric impurity). This behavior clearly indicates that the antiferromagnetic interaction is dominant in the dinuclear complex. The large Cu—O—Cu angle (126.8°) as well as distortion of the coordination geometry of Cu ions can account for the strong antiferromagnetic interactions in **4** [65–68]. This magnetic behavior agrees well with those exhibited by other alkoxo-bridged dinuclear Cu^{II} compounds with Cu—O—Cu angles >103° [63,66–73].

The diCu^{II} complex **4** is EPR silent at room temperature and 77 K, both in solution (DMSO, DMSO/H_2O) and in the solid state, due to the very strong antiferromagnetic coupling which is active in this temperature range in accordance with susceptibility measurements. The Cu$^{II}_2$ entity of **4** was further confirmed by ESI-MS in DMSO and DMSO/water solutions, where the main peaks correspond to the [Cu_2(salbutO)(solvent)]$^+$ monocations. The major peak of the ESI-mass spectrum appears at $m/z = 513.0$ ([Cu_2(salbutO)(DMSO)]$^+$,

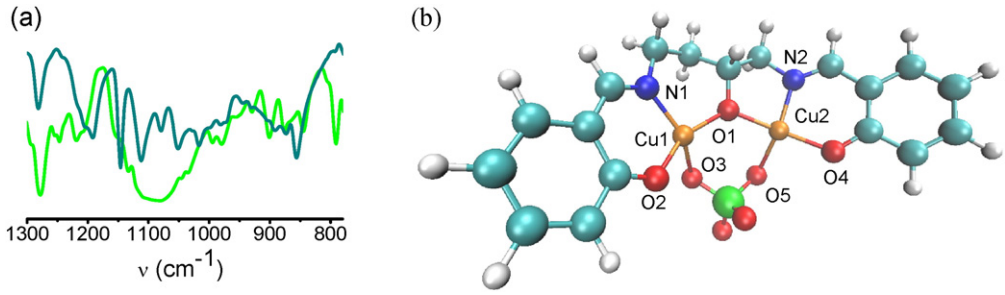

Fig. 7. (a) IR spectra of (▬) salbutOH and (▬) **4**. (b) Optimized geometry for the perchlorato bridged **4**. Calculated bond distances (Å) and angles (°): Cu(1)-N(1) 1.914, Cu(1)-O(1) 1.896, Cu(1)-O(2) 1.869, Cu(1)-O(3) 2.045, Cu(2)-N(2) 1.871, Cu(2)-O(1) 1.918, Cu(2)-O(4) 1.872, Cu(2)-O(5) 1.979; N(1)-Cu(1)-O(2) 96.4, N(1)-Cu(1)-O(3) 144.6, N(1)-Cu(1)-O(1) 101.8, O(2)-Cu(1)-O(3) 90.2, O(2)-Cu(1)-O(1) 150.3, O(3)-Cu(1)-O(1) 88.3, N(2)-Cu(2)-O(1) 86.5, N(2)-Cu(2)-O(5) 148.3, N(2)-Cu(2)-O(4) 95.8, O(1)-Cu(2)-O(5) 94.3, O(1)-Cu(2)-O(4) 159.8, O(5)-Cu(2)-O(4) 94.1.

100%) (Fig. 8), with peaks belonging to $[Cu_2(salbutO)]^+$ ($m/z = 434.8$, 33%) and $[Cu_2(salbutO)(MeOH)]^+$ ($m/z = 466.9$, 7%), also present, the last generated from coordination of the solvent employed for dilution. The isotopic patterns of these peaks match their simulated spectra very well. Peaks of mononuclear species were not observed.

3.2. XANES studies

In order to compare the site symmetry and electronic structure of the metal centers in the heterodinuclear complexes, X-ray Absorption Near Edge Structure (XANES) spectroscopic analysis was performed on complexes **1** and **3**. Due to the energetic proximity in the Cu and Zn K-edges, both edges can be recorded under the same beamtime session. The Cu *K*-edge XANES spectrum of **1** (Fig. 9(a)) shows characteristic features of a square-planar (or tetragonal) coordinated Cu^{II} ion [74,75]: a main peak at 8995 eV from the 1s to continuum transition, a shoulder on the rising edge at 8986 eV from the 1s → $4p_z$ transition + ligand to metal (3d hole) charge transfer shakedown process, and a pre-edge feature at 8978 eV from a 1s → 3d transition. Similarly, complex **3** shows a main peak at 8999 eV, a raising-edge transition at 8986 eV, and a 1s → 3d forbidden pre-edge transition at 8978 eV. The signatures of the two complexes differ at some points mirroring the different Cu^{II} environment in the two complexes, but are in line with a square-planar environment, the apical ligands, if any (coordinated ClO_4^- in **1**), being far from the metal. Comparison of the Cu *K*-edge XANES spectra of **1** and **2** are almost superimposable and thus confirms that the Cu^{II} center lies in the very same environment in the homo- and heterodinuclear complexes (Fig. 10).

In contrast to the Cu^{II} sites, the Zn^{II} atoms in **1** and **3** do not produce any pre-edge structure. The completely filled 3d shells of the zinc atom prevent 1s → 3d transitions. Instead, the Zn 1s → 4*p* transition produces an intense absorption structure, the intensity of which varies with transition probability that is related to the complex geometry. Zn *K*-edge XANES spectra of **1** and **3** are typical of a distorted tetrahedral environment of absorbing zinc with differences in the intensity and split of the edge transitions due to the presence of chloride ions in the first coordination sphere of the Zn^{II} center of **3** (Fig. 9(b)) [76]. We can distinguish three features in the XANES spectra, denoted as A, B and C. Peak A appears at 9667 eV in **1** and as a double peak at 9664 and 9666 eV in **3**. Peak B is observed at 9670 eV in **1** and as a double peak at 9671 and 9674 eV in **3**. The third feature is observed at about 9684 eV. The overall shape of the XANES spectrum of **1** is similar to bovine Cu,Zn SOD, with peaks A–B of similar intensity and the feature C as a shoulder [77], while that of **3** reflects the lower symmetry of the Zn center in this complex [78].

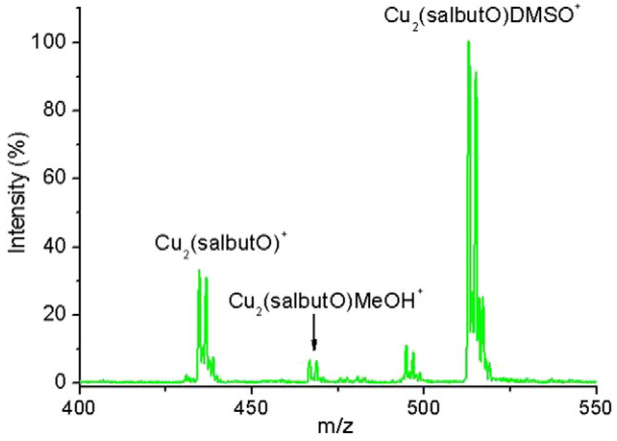

Fig. 8. ESI-Mass spectrum of **4**.

3.3. Electrochemical studies

The cyclic voltammogram (CV) of complexes **1–4** in DMF are shown in Fig. 11. DMF was chosen to measure and compare electrochemical behavior because of the high solubility of the four compounds in this solvent (**3** and **4** are slightly soluble in water). Complex **1** exhibits one

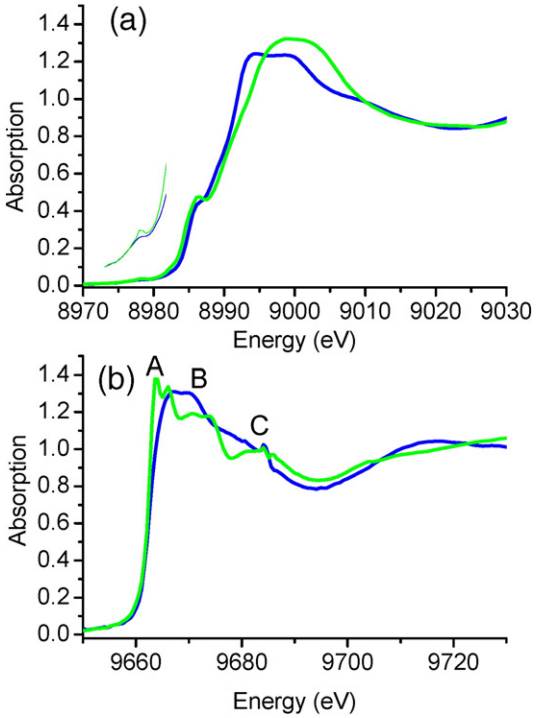

Fig. 9. Cu (a) and Zn (b) K-edge XANES spectra of **1** (▬) and **3** (▬).

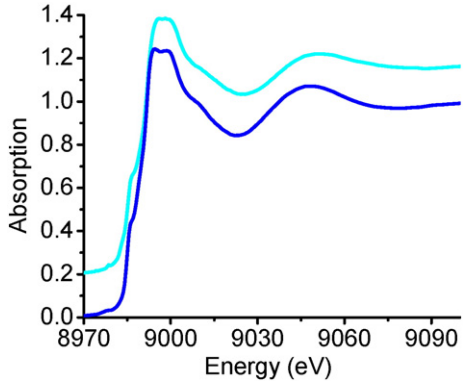

Fig. 10. Cu *K*-edge XANES spectra of **1** (▬) and **2** (▬).

cathodic wave corresponding to the Cu^{II}/Cu^{I} redox couple at E_p − 890 mV, with one associated re-oxidation wave at E_p − 360 mV corresponding to the oxidation of the chemically transformed Cu^{I} form of the complex (Fig. 11(a)). The large negative potential value is typical of Cu^{II} in square-planar geometry, and contrasts with the low negative or slightly positive redox potentials observed for Cu^{II} sites with strongly perturbed tetrahedral stereochemistry [79–81]. The measured value for the Cu^{II}/Cu^{I} couple of **1** compares well with the value of $E_p = -765$ mV found for [(dien)Cu(μ-Im)Zn(trien)] in H_2O, at pH 7 [82].

Complex **2** shows two irreversible reduction processes at $E_{p1} = -646$ and $E_{p2} = -1088$ mV, corresponding to the two one-electron $Cu^{II}{}_2/Cu^{I}Cu^{II}$ and $Cu^{I}Cu^{II}/Cu^{I}{}_2$ couples, respectively (Fig. 11(b)). After continuous cycling to a potential slightly more negative than the second reduction potential, Cu^{I} disproportionates to Cu^{II} and Cu^{0}. Deposition of Cu^{0} was confirmed by the appearance of a sharp peak in the anodic scan at 266 mV characteristic of Cu^{0} desorption from the electrode surface, the intensity of which increases after each cycle. The potential of the first reduction peak of **2** in DMF is less negative than reported in DMSO/H_2O mixtures (−760 mV vs SCE) [50], and slightly more negative than for imidazolate-bridged $diCu^{II}$ complexes of polyazamacrocyclic ligands with $J = -59$ cm^{-1}, for which reduction was observed at $E_p = -585$ mV in DMSO [83]. The redox potential of the copper ion in the native enzyme is much more positive than the potential of these complexes. This is due to the tetrahedral distortion of the copper site shown in the high resolution X-ray crystal structure [10].

The CV of complex **3** (Fig. 11(c)) shows one non-reversible wave at $E_p = -682$ (Cu^{II}/Cu^{I}) with the associated re-oxidation peak at −88 mV, and a quasi-reversible wave at $E_{1/2} = -1045$ mV ($\Delta E = 185$ mV) that can be attributed to a second one-electron reduction of the starting complex via an alternative path involving ligand-centered reduction. In the positive scan, an irreversible oxidation process is observed at ~480 mV that could be ascribed to the Cu^{II}/Cu^{III} couple [84–85], while the ligand oxidation occurs at $E_p = 1121$ mV.

Complex **4** exhibits one quasi-reversible reduction at 370 mV ($\Delta E =$ 180 mV), and one irreversible redox wave at $E_{p2} = -630$, which correspond to the $Cu^{II}{}_2/Cu^{II}Cu^{I}$ and $Cu^{II}Cu^{I}/Cu^{I}{}_2$ redox couples, respectively (Fig. 11(d)). This indicates that the two Cu^{II} ions are interacting sufficiently to make them nonequivalent. The first one-electron reduction might involve the more tetrahedrically distorted copper site (Cu(1)) facilitating the geometrical change from Cu^{II} to Cu^{I}, while the second should correspond to the Cu(2) center. It is known that the stronger the metal–metal interaction, the larger the difference in the redox *potential* values between the first and second reduction processes ($\Delta E_p = E_{p1} - E_{p2}$) [86]. In the present case, the large ΔE_p value obtained for complex **4** ($\Delta E_p = 0.9$ V) is consistent with a strong spin–spin interaction and agrees with magnetic results (see Section 3). During the reduction process a stereochemical rearrangement could occur in order to meet the co-ordination requirements of the reduced Cu^{I} center, which usually prefers trigonal planar, tetrahedral or linear stereochemistries. This stereochemical rearrangement can be accomplished through the effective partial leaving of a solvent molecule from the Cu co-ordination sphere. Since the first reduction process is quasi-reversible it is possible to assume that the stereochemical change is reversible and does not alter the identity of the original Cu^{II} complex undergoing reduction. This complex is the most easily reducible of the four complexes under study (Table S1) and this redox behavior parallels its

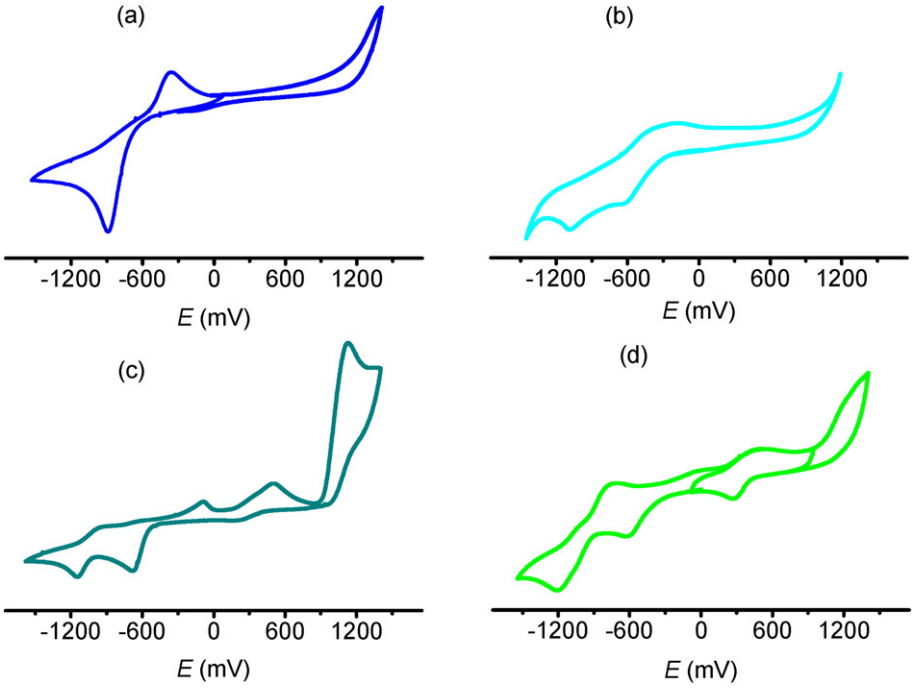

Fig. 11. Cyclic voltammograms of (a) **1**, (b) **2**, (c) **3**, and (d) **4**, in DMF. Conditions: Pt/Pt/Ag–AgCl; conc. = 1 mM; scan rate = 100 mV/s; supporting electrolyte = Bu_4NPF_6.

ability to behave as a SOD analogue (discussed below in Section 3.5). The third wave observed in the cyclic voltammogram of **4** at $E_{p2} = -1210$ mV can involve a ligand centered reduction.

3.4. Stability of complexes 1–4 in solution

The stability of complexes **1**–**4** was evaluated by EPR and UV–visible spectroscopy at different pH values.

The RT DMSO solution of **1** shows an isotropic spectrum with $g_{iso} = 2.11$ and $A_{iso} = 69 \times 10^{-4}$ cm^{-1} (Fig. 12(a)). At 120 K the complex exhibits the usual line shape for mononuclear Cu^{II} sites with $g_{//} > g_{\perp} > g_e$, indicating an axial symmetry (Fig. 12(b)). The measured values are $g_{\perp} = 2.06$, $g_{//} = 2.22$ and $A_{//} = 195 \times 10^{-4}$ cm^{-1}, with $g_{//}/A_{//} = 114$ cm, denoting a slightly distorted square-planar geometry with a d_{x2-y2} ground state. In frozen water/DMSO (1:1 *v*/v) solutions (Fig. 12(c-f)), EPR spectra of **1** keep unchanged in the narrow pH range 7.5–9.5 (shown for pH 8). At pH 10 (Fig. 12(c)), the measured $A_{//}$ values are somewhat smaller (~190×10^{-4} cm^{-1}) and $g_{//}$ increases to 2.23. Below pH 7, new features begin to appear in the spectra corresponding to Cu^{II} species formed by ligand dissociation and hydrolysis (spectrum shown for pH 6, Fig. 12(e))). At pH 2, free Cu^{2+}_{aq} dominates the spectrum as easily identified by its small $A_{//}$ of 134×10^{-4} cm^{-1} and $g_{//}$ and $g_{\perp}$ values of 2.41 and 2.085, respectively (Fig. 12(f)). When pH decreases from 7, species with $g_{//} = 2.240$ and $A_{//} = 188 \times 10^{-4}$ cm^{-1} are also observed. Lower $A_{//}$ concomitant with higher $g_{//}$ values indicate substitution of N-donor by O-donor ligands in the Cu^{II} coordination plane [82,87]. Examination of the spectra suggests that below pH 7, the starting complex converts into mononuclear $[Cu(dien)(ImH)]^{2+}$, $[Cu(dien)(H_2O)]^{2+}$ and finally Cu^{2+}_{aq}. At pH ≥ 10, hydroxide may break the imidazolate bridge to give $[Cu(dien)(OH)]^{+}$ that coexists with the starting complex.

The electronic spectrum of complex **1** in DMSO has an absorbance maximum at 605 nm ($\varepsilon = 105$ M^{-1} cm^{-1}) corresponding to the Cu^{II} d–d transition in square planar CuN_4. In 1:1 V/V DMSO:water solution of pH 8, the complex exhibits a strong band with a broad absorption maximum centered at 237 nm ($\varepsilon = 10{,}950$ M^{-1} cm^{-1}), tailing toward lower energies, which reasonably may be attributed to $N_{Ligand} \rightarrow Cu^{II}$ LMCT transitions involving the triamine and Im^{-} donor ligands [88]. At 4 < pH < 7, this band is narrower and shifts to 245 nm ($\varepsilon = 9850$ M^{-1} cm^{-1}), as imidazole is protonated and dissociated. At pH < 3, the solutions are transparent in this spectral region. The visible band of the complex shifts with pH, as shown in Fig. 12(g). At pH 8, the Cu^{II} d–d band is observed at λ_{max} 615 nm ($\varepsilon = 130$ M^{-1} cm^{-1}). At 4 < pH < 7 this band shifts to longer wavelengths (621 (pH 7), 624 (pH 6), 632 nm (pH 4)), indicating the contribution of mononuclear species resulting from imidazole dissociation and replacement by water. At pH ≤ 3 the amine ligand is also released and the spectrum is that of free cupric ion. At pH 10, the absorption at 615 nm superimposes to a band at 632 nm, the last resulting from imidazolate substitution by hydroxide.

The stability of **2** was evaluated as a function of pH in DMF/H_2O mixtures. The EPR spectrum of **2** in frozen DMF solution is displayed in Fig. 13(a). As described above, in the solid state this complex has two antiferromagnetically coupled Cu^{II} centers separated by 5.82 Å. For the $\Delta M_S = \pm 1$ transitions of the triplet state of the Cu^{II}_2 system, several peaks are predicted on either side of $g = 2$ with the overall width of the resonance determined by the Cu···Cu distance [56]. However, in frozen DMF solution, **2** exhibits an axial EPR spectrum with spectral parameters $g_{\perp} = 2.04$, $g_{//} = 2.22$, $A_{//} = 199 \times 10^{-4}$ cm^{-1}, and $g_{//}/A_{//} = 111$ cm, characteristic of uncoupled Cu^{II} in a slightly distorted square-planar geometry with a d_{x2-y2} ground state. The complex shows an analogous spectrum in DMF/H_2O frozen solution of pH 8. The lack of transitions belonging to the triplet state might arise from a different structure of the μ-imidazolate Cu^{II}_2 core in solution due to crystal packing effects in the solid state. In particular, if the dihedral angle (α angle between the imidazolate ring and the copper coordination plane) is affected, a significant difference for J is expected (in the present case, $J_{solution} \ll J_{solid}$). A similar behavior had already been observed in DMSO and DMSO/H_2O mixtures [50].

The electronic spectrum of complex **2** in DMF shows an intense *CT* band at 250 nm ($\varepsilon = 8010$ M^{-1} cm^{-1}) and a weak band at 593 nm ($\varepsilon = 223$ M^{-1} cm^{-1}) corresponding to the Cu^{II} d–d transition in square planar CuN_4 (Fig. 13(b)). The visible band shifts with pH as shown in Fig. 13(c–g). At pH 8, the band is observed at λ_{max} 595 nm ($\varepsilon = 130$ M^{-1} cm^{-1}), and remains stable at least during 5 h. At pH < 7 this band shifts to longer wavelengths (611 (pH 7), 620 (pH 5)), indicating the contribution of mononuclear species resulting from protonation and substitution of imidazole by water. At pH > 10, the absorption at 595 nm broadens and superimposes to a band at 632 nm resulting from imidazolate substitution by hydroxide. These results differ from

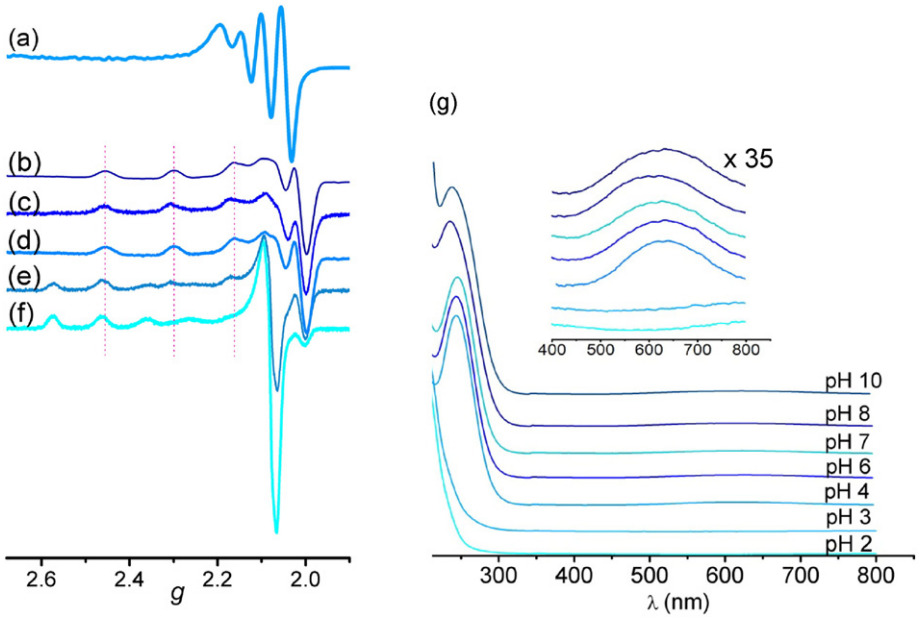

Fig. 12. X-band EPR spectra of **1** in (a) DMSO, 300 K, (b) DMSO, 120 K; and 1:1 DMSO/H_2O mixtures at (c) pH 10; (d) pH 8; (e) pH 6; (f) pH 2. (g) Electronic spectra of **1** in 1:1 V/V DMSO/H_2O mixtures at different pH. [**1**] = 1.46×10^{-3} M.

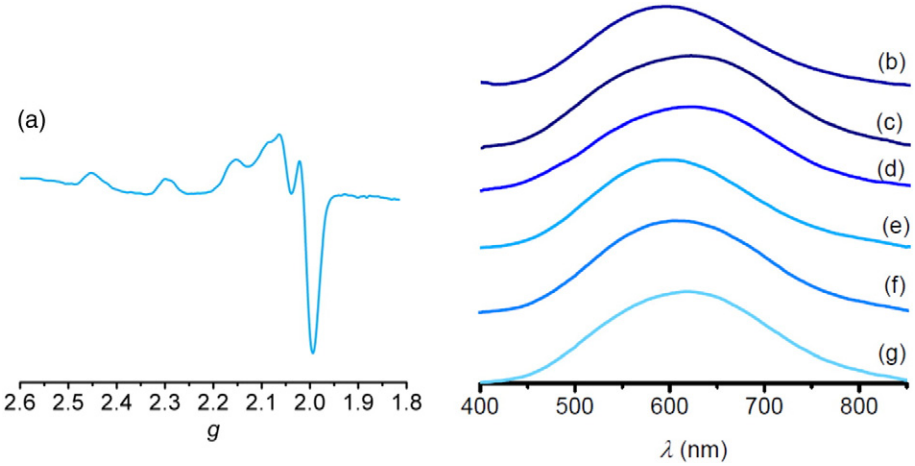

Fig. 13. (a) X-band EPR spectrum of **2** in frozen DMF solution. Electronic spectra of **2** in DMF (b), 1:1 DMF/H_2O solution of pH 11.5 (c), 10 (d), 8 (e), 7 (f) and 5 (g). [**2**] = 7.15×10^{-4} M.

those obtained for this complex in DMSO/H_2O mixtures, where the complex was found to be stable in the 7.75–12.5 pH range [50]. Differences are especially significant at high pH where the absorption bands clearly show the formation of hydroxo species, as observed by the same authors for the Me-Im-bridged diCu^{II} analogue, which is stable in the 7–10 pH range [38].

As described above, the $ZnCl_2$ moiety of complex **3** dissociates in DMSO, and the $[Cu(salpn)]_2$ dimer is formed. Dimerization is not observed in DMSO/water mixtures. EPR spectra of frozen DMSO/water solutions of this complex show the axial symmetry typical of mononuclear Cu^{II} sites (Fig. 14(a)). In the 5–10 pH range, the spectra remain unchanged with $g_{//} = 2.25$, $A_{//} = 185 \times 10^{-4}$ cm^{-1}, $g_{\perp} = 2.05$, and $g_{//}/A_{//} = 122$ cm, corresponding to Cu^{II} in slightly distorted square-planar geometry with a d_{x2-y2} ground state. At lower pH values, a signal with $g_{//} = 2.42$, $g_{\perp} = 2.08$ and $A_{//} = 120$ cm^{-1}, characteristic of Cu^{2+}_{aq}, appears and ultimately dominates the spectrum at pH 2.

The electronic spectrum of **3** in DMSO (Fig. 14(b)) exhibits an intense CT band at 385 nm and a broad unsymmetrical band attributed to Cu^{II} d–d transitions with $\lambda_{max} = 613$ nm ($\varepsilon = 169$ M^{-1} cm^{-1}). In DMSO/H_2O mixtures, the visible band shifts to 590 nm and remains unchanged in the 5.5–10 pH range (Fig. 14(c–e)), showing a tail on its low energy side. A band-shift to lower wavelengths as the basicity of the solvent decreases had already been observed for [Cu(salen)] complexes [89]. When the pH drops to 2.7, the intensity of this band decreases to one half of the value at pH 7, indicating that ligand dissociation takes place to a considerable extent, in agreement with EPR results (Fig. 14(f)).

Complex **4** is EPR silent in DMSO and DMSO/water mixtures of pH > 7, consistent with the occurrence of strong antiferromagnetic coupling between the bridged Cu^{II} ions, and evidences that the complex remains dinuclear in solution. Below pH 7, spectral features of uncoupled Cu^{II} begin to appear, probably as a result of the protonation of the central alkoxo bridge and disruption of the Cu—Cu spin interaction. At pH 4 (Fig. 15(a)) the spectrum shows superimposition of at least two species, with $g1_{//} = 2.26$, $A1_{//} = 180 \times 10^{-4}$ cm^{-1} and $g1_{\perp} = 2.06$, and $g2_{//} = 2.41$, $A2_{//} = 120 \times 10^{-4}$ cm^{-1} and $g2_{\perp} = 2.08$, respectively. At pH 2, Cu^{2+}_{aq} dominates the spectrum.

EPR parameters of the four complexes at pH 8 are summarized in Table S2.

The electronic spectrum of **4** in DMSO (Fig. 15(b)) shows a strong intraligand band at 270 nm, an intense *CT* band at 385 nm ($\varepsilon = 4100$ M^{-1} cm^{-1}) and a weak d–d transition centered at 620 nm ($\varepsilon = 268$ M^{-1} cm^{-1}). In 1:1 DMSO/H_2O solution of pH 7.5–10, the *CT* and d–d transitions shift to 371 and 592 ($\varepsilon = 265$ M^{-1} cm^{-1}) nm, respectively, as a result of solvatochromic effects. In the aqueous medium, the visible wave shows a tail on its low-energy side. These features are

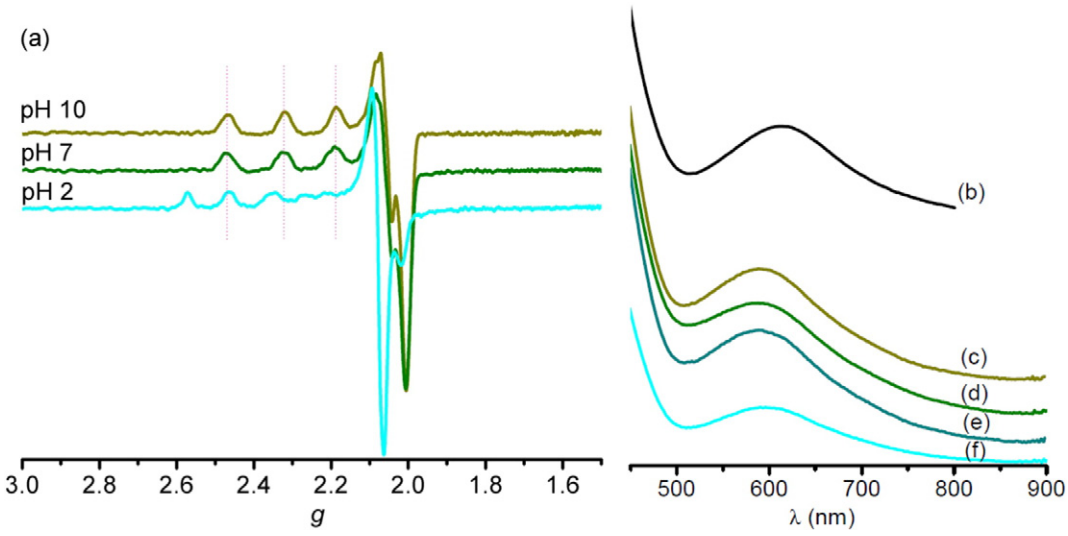

Fig. 14. (a) X-band EPR spectra of **3** in frozen 1:1 (V/V) DMSO/H_2O solutions of different pH and $T = 120$ K. Electronic spectra of **3** in DMSO (b) and in 1:1 (V/V) DMSO/H_2O solution of pH 10 (c), 7.0 (d), 5.5 (e) and 2.7 (f). [**3**] = 7.1×10^{-4} M.

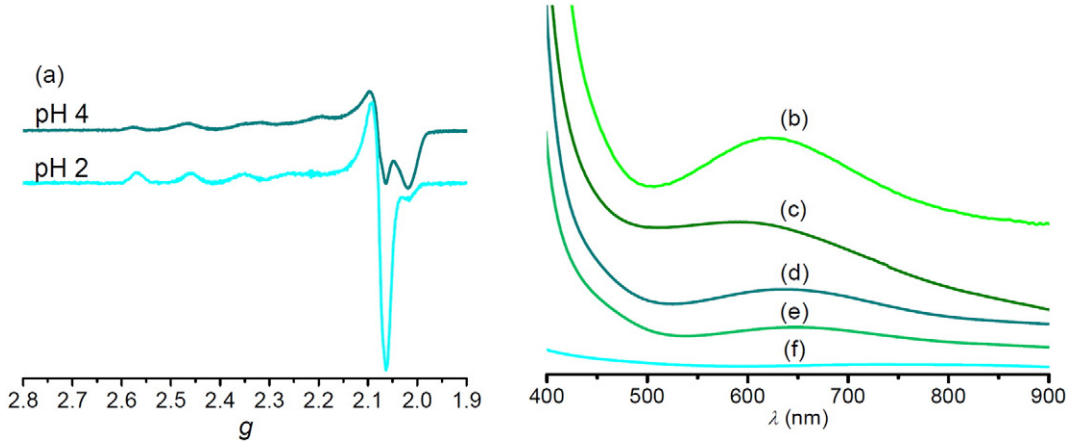

Fig. 15. (a) X-band EPR spectra of **4** in 1:1 (V/V) DMSO/H_2O frozen solutions. $T = 120$ K. Electronic spectra of **4** in DMSO (b), 1:1 DMSO/H_2O solution of pH 8 (c), 7 (d), 4 (e) and 2 (f). [**4**] = 4.1×10^{-4} M.

characteristic of $diCu^{II}$ complexes with the metal centers in tetrahedrically distorted square-planar geometry [69,73,90]. As pH decreases below 7, the weak d–d band shifts to lower energies (636 nm at pH 7, 642 nm at pH 4) and its intensity diminishes probably due to changes in the geometry around the Cu^{II} ions as protonated donor groups of the ligand are replaced by water molecules [91], together with the formation of Cu^{2+}_{aq}, which is again the major species at pH 2.

3.5. SOD activity

The SOD activity of complexes **1**–**4** was measured by the Beauchamps and Fridovich assay using the NBT reagent, at pH 7.8. The complexes' stability was checked by UV–vis spectroscopy in the aqueous phosphate buffer employed for the SOD test. Electronic spectra of complexes **1**–**4**, with and without addition of methionine, registered at different time–lengths (up to 30 min) after preparation of the solution were identical (Figs. S2, S3), revealing that the compounds are stable in the buffer, and well different from the spectrum of Cu^{2+}_{aq} in this medium (Fig. S4). The already discussed pH dependent EPR and UV–vis studies indicated that, with the exception of complex **3** which most probably exists as [Cu(salpn)], complexes **1**, **2** and **4** retain their dinuclear entities at pH 7.8. The measured IC_{50} values (concentrations of complexes required to attain 50% inhibition of the superoxide reduction) and calculated rate constants (k_{McF}) are listed in Table 3 (note that the smaller the IC_{50} value, the higher the SOD activity) together with other complexes previously evaluated using indirect methods. The four complexes exhibit activity toward the dismutation of superoxide anion with relative SOD rates: **4** > **2** > **1** > **3** (Fig. S1). The high activity of **4** parallels its ability to be reduced to the $Cu^{II}Cu^{I}$ oxidation state, which is higher than for complexes **1**, **2** and **3** where the N_4- or N_2O_2-

Table 3
SOD activity of complexes **1**–**4** and other SOD mimics.

	Complex	IC_{50} (μM)	$10^6 \times k_{McF}$ (M^{-1} s^{-1})	Method
1	$[CuZn(dien)_2(\mu\text{-Im})](ClO_4)_3$ (**1**)	0.423	6.46	pH 7.8[a]
2	$[Cu_2(dien)_2(\mu\text{-Im})](ClO_4)_3$ (**2**)	0.35	7.80	pH 7.8[a]
3	$[CuZn(salpn)Cl_2]$ (**3**)	3.2	0.85	pH 7.8[a]
4	$[Cu_2(salbutO)(ClO_4)]$ (**4**)	0.102	26.8	pH 7.8[a]
5	$[CuZn(bdpi)(CH_3CN)_2](ClO_4)_3$	0.24 [27]	25[e]	pH 7.8[b]
6	$[Cu_2(bdpi)(CH_3CN)_2](ClO_4)_3$	0.32 [27]	18.8[e]	pH 7.8[b]
7	$[(Cu(\mu\text{-Im})ZnL_{\text{-2H}})(Cu(\mu\text{-Im})ZnL_{\text{-H}})](ClO_4)_3$	0.26 [25]	23[e]	pH 7.8[c]
8	$[(Cu(\mu\text{-Im})Cu)L]ClO_4$	0.62 [25]	9.68[e]	pH 7.8[c]
9	$[(pip)Cu(\mu\text{-Im})Zn(pip)](NO_3)_3$	0.5 [92]	7.9[e]	pH 7.8[c]
10	$[(pip)Cu(\mu\text{-Im})Cu(pip)](NO_3)_3$	0.5 [92]	7.9[e]	pH 7.8[c]
11	$[(en)_2Cu(\mu\text{-Im})Cu(en)_2](ClO_4)_3$	52 [20]	0.18[e]	pH 8.6[d]
12	$[CuZnL^1(\mu\text{-Im})](ClO_4)_3$	1.57 [23]	0.18[e]	pH 7.8[a]
13	$[(dien)Cu(\mu\text{-Im})Zn(tren)](ClO_4)_3$	69 [93]	0.145[e]	pH 7.0[a]
14	$[Cu_2L^1(\mu\text{-Im})](ClO_4)_3$	1.96 [23]	0.14[e]	pH 7.8[a]
15	$[CuZnL^2(\mu\text{-Im})]$	3 [94]	0.08[e]	pH 7.8[c]
16	$[(PMDT)Cu(\mu\text{-Im})Zn(PMDT)](ClO_4)_3$	45 [46]	0.015[e]	pH 8.6[d]
17	$[(PMDT)Cu(\mu\text{-Im})Cu(PMDT)](ClO_4)_3$	48 [47]	0.014[e]	pH 8.6[d]
18	$[(tren)Cu(\mu\text{-}E\text{-Im})Cu(tren)](ClO_4)_3$	85 [95]	0.011[e]	pH 8.6[d]
19	$[Cu(Pu\text{-}6\text{-}MePy)(H_20)]^{2+}$	2.25 [17]	6.3[e]	pH 8.0[c]
20	[Cu(5-EtO-salpn)$ZnCl_2$]	1.31 [13]	2.1[e]	pH 7.4[a]
21	$[CuL^3ZnCl_2]$	3.127 [14]	0.87[e]	pH 7.4[a]
22	Cu,Zn- SOD	0.03 [92]	1300 [76]	pH 7.8[c]

Hbdpi = 4.5-bis(di(2-pyridylmethyl)aminomethyl)imidazole; L = 3,6,9,16,19,22-hexaaza-6,19-bis(2-hydroxyethyl)tricyclo[22,2,2,$2^{11,14}$]triaconta-1,11,13,24,27,29-hexaene); Pip = [2(2-pyridyl)ethylaminomethyl]pyridine; L^1 = 3,6,9,16,19,22-hexaaza-6,19-bis(1H-imidazol-4-ylmethyl)tricycle[22,2,2,$2^{11,14}$]triaconta-1,11,13,24,27,29-hexaene; L^2 = 5,5″-pentaazaterpyridinophane; PMDT = pentamethyldiethylenetriamine; E-ImH = 2-ethylimidazole; tren = tris(2-amino-ethyl)amine; Pu-6-MePy = *N*,*N*′-bis(2-(6-methylpyridyl)methylene)-1,4-butanediamine; L^3 = *N*,*N*′-bis(4-methoxysalicylidene)cyclohexane-1,2-diamine.

[a] Riboflavin–methionine–NBT assay.
[b] Xanthine–xanthine oxidase–cytochrome *c* assay.
[c] Xanthine–xanthine oxidase–NBT assay.
[d] NaOH/DMSO-NBT assay.
[e] Values calculated from reported experimental data as $k_{McF} = k_{indicator}$ [indicator] / IC_{50}. Values used for $k_{NBT} = 5.9 \times 10^4$ M^{-1} s^{-1} [30,96] and $k_{cyt\ c} = 6 \times 10^5$ M^{-1} s^{-1} [97].

donor set from the ligands is disposed in a nearly square-planar geometry around the metal ion. Besides, in aqueous solution ClO_4^- dissociates from complex **4**, leaving each Cu ion tricoordinated to the $O_{Ph}N_{im}O_{ol}$ donor set of salbutO^{3-} with the fourth coordination position occupied by a labile solvent molecule, which turns this complex more appropriate to act as a SOD mimic. Assuming that the redox cycle involves Cu^{II}/Cu^{I} oxidation states, the known preference of Cu^{I} for a trigonal–planar or tetrahedral geometry supports the superior activity shown by complex **4**. Imidazolate-bridged complexes (**1**, **2**), although effective to scavenge $O_2^{\bullet-}$, react 3–4-times slower than **4** as a consequence of the higher geometrical changes required during the reaction. In addition, the two imidazolate-bridged complexes react at similar rate, revealing that Zn^{II} has little or no effect on the rate of these SOD mimics. Electrochemical properties of **3** show this complex is easier to oxidize than **1**, **2** and **4**. However, the low SOD activity of **3** suggests that the Cu^{II}/Cu^{III} couple is not involved in the redox cycle. These results show that an effective $O_2^{\bullet-}$ disproportionation reaction can be fulfilled even when the potential of the Cu^{II}/Cu^{I} couple of the complex is not between redox potentials for $O_2/O_2^{\bullet-}$ (−0.397 V vs Ag/AgCl) and $O_2^{\bullet-}/H_2O_2$ (+0.653 V vs Ag/AgCl), although activity is considerably improved when the Cu^{II}/Cu^{I} couple is within this potential range.

On the basis of competition with the indicator, at 50% inhibition, the rates of the reactions of indicator (NBT in the present study) and the mimic with $O_2^{\bullet-}$ are equal, k_{McF} [complex] = $k_{indicator}$ [indicator]. Hence, the calculated rate constants, $k_{McF} = k_{indicator}$ [indicator] / IC_{50}, are independent of the detector concentration and appropriate for comparison with literature values. In the third column of Table 3 k_{McF}, calculated from published IC_{50} values and [indicator], are listed for several SOD mimics. Cu,Zn and diCu complexes with Cu coordinated to three or four donor sites of the ligand and the fourth/fifth position occupied by one labile molecule or group are the most active (Table 3, entries 1–2, 4–10). Among them, dinucleating or macrocyclic ligands (Table 3, entries 4, 5–8) afford more effective compounds than imidazole + capping ligand systems. Complexes in which Cu binds five donor sites of the ligand (Table 3, entries 11–12, 14, 18), or the ligand imposes rigidity making difficult the molecular rearrangement along the reaction pathway (Table 3, entry 15) or alkyl substituents impose steric effects hindering the access of superoxide to the metal center (Table 3, entries 16–17), show moderate SOD activity. The SOD activity observed for [(dien)Cu(μ-Im)Zn(tren)](ClO$_4$)$_3$ (Table 3, entry 13) is lower than for complexes **1** and **2** probably because of the lower pH used in the SOD test. The Schiff-base complex [Cu(Pu-6-MePy)($H_2$0)]$^{2+}$ with a distorted trigonal bipyramidal $N_4O_{(H2O)}$ geometry around the Cu ion (Table 3, entry 19) shows SOD activity similar to complexes **1** and **2**, and is 3- to 7-times more active than Schiff-base complexes with a nearly square-planar CuN_2O_2 center (Table 3, entries 3, 20–21). Although all tested complexes are active, the k_{McF} values of the best mimics are still two orders of magnitude smaller than reported for native Cu,Zn-SOD (Table 3, entry 22).

4. Conclusions

[CuZn(dien)$_2$(μ-Im)](ClO$_4$)$_3$ (**1**) and [Cu$_2$(dien)$_2$(μ-Im)](ClO$_4$)$_3$ (**2**) can be obtained as pure solids only when the pH is controlled to values ≥11 and 9, respectively. At pH 9, the reaction of [Cu(dien)(ImH)](ClO$_4$)$_2$ with [Zn(dien)(H$_2$O)](ClO$_4$)$_2$ affords the Cu$_3$Zn tetranuclear complex [{(dien)Cu(μ-Im)}$_3$Zn(OH$_2$)(ClO$_4$)$_2$](ClO$_4$)$_3$ (**1a**) as the main reaction product. Heterodinuclear [CuZn(salpn)Cl$_2$] (**3**) forms [Cu(salpn)]$_2$ dimers in DMSO solution, which dissociate in aqueous medium. [Cu$_2$(salbutO)ClO$_4$] (**4**) possesses a strong antiferromagnetically coupled alkoxo-bridged diCu^{II} unit, in either the solid state and solution, and is reduced to the mixed valence $Cu^{II}Cu^{I}$ oxidation state more easily than the other three complexes under study.

Complexes **1**, **2** and **4** retain their dinuclearity in aqueous medium around physiological pH, while **3** most probably exists as [Cu(salpn)]. The riboflavin–methionine system used in this work to generate $O_2^{\bullet-}$ supplies a low and stationary amount of $O_2^{\bullet-}$ that provides a way to differentiate the scavenging ability of these compounds. Therefore, the four complexes are able to disproportionate $O_2^{\bullet-}$ in aqueous medium at pH 7.8, but with different rates. The diCu^{II} complex of the dinucleating Schiff-base ligand salbutO^{3-} (**4**) is more active than the imidazolate-bridged diCu and Cu,Zn complexes (**1** and **2**), and much better than complex **3** formed with salpn. Interestingly, [Cu$_2$(salbutO)]$^+$ exhibits the highest activity among the SOD models reported so far. Several factors can favor the disproportionation of $O_2^{\bullet-}$ by this complex, such as the ability of salbutO^{3-} to accommodate the copper ion in both Cu^{I} and Cu^{II} states because of its degree of flexibility, and the lability of the fourth coordination position of copper that facilitates stereochemical rearrangement to meet a trigonal planar co-ordination around the Cu^{I} center. The present results encourage the evaluation of the SOD activity of other ring-substituted salbutO^{3-} diCu complexes with Cu^{II}/Cu^{I} redox potentials modulated to values closer to the midpoint potential between the reduction and oxidation of $O_2^{\bullet-}$ ($E_{1/2}$ = 0.12 V vs. Ag/AgCl).

Abbreviations

IC_{50}	concentration for 50% inhibition
CV	cyclic voltammogram
Dien	diethylenetriamine
DtmaH	4-diethylenetriamineacetic acid
E-ImH	2-ethylimidazole
ESI-MS	electrospray ionization mass spectrometry
Hbdpi	4,5-bis(di(2-pyridylmethyl)aminomethyl)imidazole
H_2salbutO	1,4-bis(salicylideneamino)butane
H_2salpn	1,3-bis(salicylidenamino)propane
Im	imidazole
k_{McF}	McCord–Fridovich' rate constant
L	3,6,9,16,19,22-hexaaza-6,19-bis(2-hydroxyethyl)tricyclo[22,2,2,2^{11,14}]triaconta-1,11,13,24,27,29-hexaene)
L^1	3,6,9,16,19,22-hexaaza-6,19-bis(1H-imidazol-4-ylmethyl)tricyclo[22,2,2,2^{11,14}] triaconta-1,11,13,24,27,29-hexaene
L^2	5,5″-pentaazaterpyridinophane
L^3	*N*,*N*′-bis(4-methoxysalicylidene)cyclohexane-1,2-diamine
LMCT	ligand-to metal charge transfer
NBT	nitro blue tetrazolium
Pip	[2(2-pyridyl)ethylaminomethyl]pyridine
PMDT	pentamethyldiethylenetriamine
Pu-6-MePy	*N*,*N*′-bis(2-(6-methyl-pyridyl)methylene)-1,4-butanediamine
ROS	reactive oxygen species
SOD	superoxide dismutase
Trien	triethylenetetramine
Tren	tris(2-amino-ethyl)amine
XANES	X-ray absorption near edge structure

Acknowledgments

We thank the National University of Rosario and CONICET for financial support (PIP 0335) and CONICET–CNRS for a bilateral agreement (Res. 991/2013). We acknowledge the ESRF for provision of synchrotron radiation on the FAME beamline (Proposal 30-02-1078), the FAME team and Drs. F. Collin, S. Sayen, Prof. E. Guillon and C. Cheignon for their participation in data recording.

Appendix A. Supplementary data

Crystallographic data for the structures reported in this paper have been deposited with the Cambridge Crystallographic Data Center as Supplementary Publication No. CCDC-1455727 (**1a**) and CCDC-

1455728 (**3**). Supplementary data associated with this article can be found in the online version, at http://dx.doi.org/10.1016/j.jinorgbio.2016.07.008.

References

[1] Y. Sheng, I.A. Abreu, D.E. Cabelli, M.J. Maroney, A.-F. Miller, M. Teixeira, J.S. Valentine, Chem. Rev. 114 (2014) 3854–3918.
[2] D.P. Riley, Chem. Rev. 99 (1999) 2573–2587.
[3] I. Batinic-Haberle, S. Reboucas Julio, I. Spasojevic, Antioxid. Redox Signal. 13 (2010) 877–918.
[4] J.M. McCord, M.A. Edeas, Biomed. Pharmacother. 59 (2005) 139–142.
[5] D. Salvemini, C. Muscoli, D.P. Riley, S. Cuzzocrea, Pulm. Pharmacol. Ther. 15 (2002) 439–447.
[6] S. Cuzzocrea, D.P. Riley, A.P. Caputi, D. Salvemini, Pharmacol. Rev. 53 (2001) 135–159.
[7] R.H. Burdon, Free Radic. Biol. Med. 18 (1995) 775–794.
[8] I.A. Abreu, D.E. Cabelli, Biochim. Biophys. Acta 1804 (2010) 263–274.
[9] R.W. Strange, S. Antonyuk, M.A. Hough, P.A. Doucette, J.A. Rodriguez, P.J. Hart, L.J. Hayward, J.S. Valentine, S.S. Hasnain, J. Mol. Biol. 328 (2003) 877–891.
[10] J.A. Tainer, E.D. Getzoff, K.M. Beem, J.S. Richardson, D.C. Richardson, J. Mol. Biol. 160 (1982) 181–217.
[11] C. Muscoli, S. Cuzzocrea, D.P. Riley, J.L. Zweier, C. Thiemermann, Z.-Q. Wang, D. Salvemini, Br. J. Pharmacol. 140 (2003) 445–460.
[12] O. Iranzo, Bioorg. Chem. 39 (2011) 73–87.
[13] C. Wang, S. Li, D.-J. Shang, X.-L. Wang, Z.-L. You, H.-B. Li, Bioorg. Med. Chem. Lett. 21 (2011) 4320–4324.
[14] Z.L. You, L.L. Ni, P. Hou, J.C. Zhang, C. Wang, J. Coord. Chem. 63 (2010) 515–523.
[15] J. Han, Y. Xing, C. Wang, P. Hou, F. Bai, X. Zeng, X. Zhang, M. Ge, J. Coord. Chem. 62 (2009) 745–756.
[16] R.N. Patel, V.L.N. Gundla, D.K. Patel, Polyhedron 27 (2008) 1054–1060.
[17] J. Müller, D. Schübl, C. Maichle-Mössmer, J. Strähle, U. Weser, J. Inorg. Biochem. 75 (1999) 63–69.
[18] Z.-P. Qi, K. Cai, Q. Yuan, T.-A. Okamura, Z.-S. Bai, W.-Y. Sun, N. Ueyama, Inorg. Chem. Commun. 13 (2010) 847–851.
[19] H. Fu, Y.-H. Zhou, W.-L. Chen, Z.-G. Degin, M.-L. Tong, L.-N. Ji, Z.-W. Mao, J. Am. Chem. Soc. 128 (2006) 4924–4925.
[20] R.N. Patel, N. Singh, K.K. Shukla, V.L.N. Gundla, U.K. Chauhan, J. Inorg. Biochem. 99 (2005) 651–663.
[21] G. Tabbi, W.L. Driessen, J. Reedijk, R.P. Bonomo, N.O. Veldman, A.L. Speek, Inorg. Chem. 36 (1997) 1168–1175.
[22] K.G. Strothkamp, S.J. Lippard, Acc. Chem. Res. 10 (1982) 318–326.
[23] Q. Yuan, K. Cai, Z.-P. Qi, Z.-S. Bai, Z. Su, W.-Y. Sun, J. Inorg. Biochem. 103 (2009) 1156–1161.
[24] B. Boka, A. Myari, I. Sóvágó, N. Hadjiliadis, J. Inorg. Biochem. 98 (2004) 113–122.
[25] D. Li, S. Li, D. Yang, J. Yu, J. Huang, Y. Li, W. Tang, Inorg. Chem. 42 (2003) 6071–6080.
[26] J.L. Pierre, Chem. Soc. Rev. 29 (2000) 251–257.
[27] H. Ohtsu, Y. Shimazaki, A. Odani, O. Yamauchi, W. Mori, S. Itoh, S. Fukuzumi, J. Am. Chem. Soc. 122 (2000) 5733–5741.
[28] D.P. Riley, W.J. Rivers, R.H. Weiss, Anal. Biochem. 196 (1991) 344–349.
[29] W.F. Beyer Jr., I. Fridovich, Anal. Biochem. 161 (1987) 559–566.
[30] S. Durot, C. Policar, F. Cisnetti, F. Lambert, J. Renault, G. Pelosi, G. Blain, H. Korri-Youssoufi, J. Mahy, Eur. J. Inorg. Chem. (2005) 3513–3523.
[31] R.F. Pasternack, B. Halliwell, J. Am. Chem. Soc. 101 (1979) 1026–1031.
[32] O. Proux, X. Biquard, E. Lahera, J.J. Menthonnex, A. Prat, O. Ulrich, Y. Soldo, P. Trévisson, G. Kapoujvan, G. Perroux, P. Taunier, D. Grand, P. Jeantet, M. Deleglise, J.-P. Roux, J.-L. Hazemann, Phys. Scr. 115 (2005) 970–973.
[33] O. Proux, V. Nassif, A. Prat, O. Ulrich, E. Lahera, X. Biquard, J.J. Menthonnex, J.-L. Hazemann, J. Synchrotron Radiat. 13 (2006) 59–68.
[34] M.J. Frisch, et al., Gaussian 09, Revision D.01, Gaussian, Inc., Wallingford, CT, 2009.
[35] A.D. Becke, J. Chem. Phys. 98 (1993) 5648–5652.
[36] P.J. Stephens, F.J. Devlin, C.F. Chabalowski, M.J. Frisch, J. Phys. Chem. 98 (1994) 11623–11627.
[37] R.N. Patel, H.C. Pandey, K.B. Pandeya, Synth. React. Inorg. Met.-Org. Chem. 29 (1999) 1733–1745.
[38] R.N. Patel, S. Kumar, K.B. Pandeya, P.V. Khadikar, Spectrochim. Acta A 58 (2002) 2961–2969.
[39] L. Murase, S. Ueno, S. Kida, Inorg. Chim. Acta 87 (1984) 155–157.
[40] C. Beauchamps, I. Fridovich, Anal. Biochem. 44 (1971) 276–287.
[41] Bruker, APEX2 and SAINT, Bruker AXS Inc., Madison, WI, 2008.
[42] G.M. Sheldrick, Acta Crystallogr. A64 (2008) 112–122.
[43] L.J. Farrugia, J. Appl. Crystallogr. 45 (2012) 849–854.
[44] D.M. Watkin, L. Pearce, C.K. Prout, A Molecular Graphics Package, Chemical Crystallography Laboratory, University of Oxford, 1993.
[45] Z.-W. Mao, M.-Q. Chen, X.-S. Tan, J. Liu, W.-X. Tang, Inorg. Chem. 34 (1995) 2889–2893.
[46] Z.-W. Mao, D. Chen, W.-X. Tang, K.-B. Yu, L. Liu, Chin. J. Chem. 10 (1992) 45–51.
[47] R.N. Patel, S. Kumar, K.B. Pandeya, J. Inorg. Biochem. 89 (2002) 61–68.
[48] Q. Lu, Q.H. Luo, A.B. Dai, Z.Y. Zhou, G.Z. Hu, J. Chem. Soc. Chem. Commun. (1990) 1429–1430.
[49] S. Mondal, S. Mandal, L. Carrella, A. Jana, M. Fleck, A. Köhn, E. Rentschler, S. Mohanta, Inorg. Chem. 54 (2015) 117–131.
[50] R.N. Patel, N. Singh, K.K. Shukla, U.K. Chauhan, Spectrochim. Acta A 61 (2005) 287–297.
[51] R.N. Patel, N. Singh, K.K. Shukla, U.K. Chauhan, CCDC 203653: Experimental Crystal Structure Determination, 2005.
[52] B. Bleaney, K.D. Bowers, Proc. R. Soc. Lond. Ser. A 214 (1952) 451–465.
[53] D.-X. Yang, S.-A. Li, D.-F. Li, M. Chen, J. Huang, W.-X. Tang, Polyhedron 22 (2003) 925–932.
[54] L. Tatar, O. Atakol, D. Ulku, M. Aksu, Acta Cryst C55 (1999) 923–925.
[55] Z.-L. You, Y. Lu, N. Zhang, B.-W. Ding, H. Sun, P. Hou, C. Wang, Polyhedron 30 (2011) 2186–2194.
[56] T.D. Smith, J.R. Pilbrow, Coord. Chem. Rev. 13 (1974) 173–278.
[57] G. Verquin, G. Fontaine, E. Abi-Aad, E. Zhilinskaya, A. Aboukaïs, J.-L. Bernier, J. Photochem. Photobiol. B 86 (2007) 272–278.
[58] O. Ibopishak Singh, M. Damayanti, N. Rajen Singh, R.K. Hemakumar Singh, M. Mohapatra, R.M. Kadam, Polyhedron 24 (2005) 909–916.
[59] S. Amani Komaei, G.A. van Albada, J.G. Haasnoot, H. Kooijman, A.L. Spek, J. Reedijk, Inorg. Chim. Acta 286 (1999) 24–29.
[60] Y. Nishida, S. Kida, J. Chem. Soc. Dalton Trans. (1986) 2633–2640.
[61] T. Kawata, M. Yamanaka, S. Ohba, Y. Nishida, M. Nagamatsu, T. Tokii, M. Kato, O.W. Steward, Bull. Chem. Soc. Jpn. 65 (1992) 2739–2749.
[62] C. Li, N. Kanehisa, Y. Miyagi, Y. Nakao, S. Takamizawa, W. Mori, Y. Kai, Bull. Chem. Soc. Jpn. 70 (1997) 2429–2436.
[63] D. Ghosh, N. Kundu, G. Maity, K.-Y. Choi, A. Caneschi, A. Endo, M. Chaudhury, Inorg. Chem. 43 (2004) 6015–6023.
[64] Y. Elerman, A. Elmali, Z. Naturforsch. 56 (b) (2001) 970–974.
[65] L. Merz, W. Haase, J. Chem. Soc. Dalton Trans. 875-880 (1980).
[66] S. Akine, A. Akimoto, T. Shiga, H. Oshio, T. Nabeshima, Inorg. Chem. 47 (2008) 875–885.
[67] P. Bhowmik, N. Aliaga-Alcalde, V. Gómez, M. Corbella, S. Chattopadhyay, Polyhedron 49 (2013) 269–276.
[68] H.P. Walz, W. Haase, J. Chem. Soc. Dalton Trans. (1985) 913–920.
[69] M. Gonzalez-Alvarez, G. Alzuet, J. Borrása, S. García-Granda, J.M. Montejo-Bernardo, J. Inorg. Biochem. 96 (2003) 443–451.
[70] F. Zippel, F. Ahlers, R. Werner, W. Haase, H.F. Nolting, B. Krebs, Inorg. Chem. 35 (1996) 3409–3419.
[71] M.G.B. Drew, P. Yates, F.S. Esho, J. Trocha-Grimshaw, A. Lavery, K.P. McKillop, S.M. Nelson, J. Nelson, J. Chem. Soc. Dalton Trans. (1988) 2995–3003.
[72] J.F. Wishart, C. Ceccarelli, R.L. Lintvedt, J.M. Berg, D.P. Foley, T. Frey, J.E. Hann, K.O. Hodgson, R. Weiss, Inorg. Chem. 22 (1983) 1667–1671.
[73] G.A. van Albada, M.T. Lakin, N. Veldman, A.L. Spek, J. Reedijk, Inorg. Chem. 34 (1995) 4910–4917.
[74] T.A. Smith, J.P. Penner-Hahn, M.A. Berding, S. Doniach, K.O. Hodgson, J. Am. Chem. Soc. 107 (1985) 5945–5955.
[75] L.S. Kau, D.J. Spira-Solomon, J.E. Penner-Hahn, K.O. Hodgson, E.I. Solomon, J. Am. Chem. Soc. 109 (1987) 6433–6442.
[76] F.A. Cotton, H.P. Hanson, J. Chem. Phys. 28 (1958) 83–87.
[77] L.M. Murphy, R.W. Strange, S.S. Hasnain, Structure 5 (1997) 371–379.
[78] W. Liu, S. Borg, B. Etschmann, Y. Mei, J. Brugger, Chem. Geol. 298/299 (2012) 57–69.
[79] S. Timári, R. Cerea, K. Várnagy, J. Inorg. Biochem. 105 (2011) 1009–1017.
[80] R.P. Bonomo, G. Impellizzeri, G. Pappalardo, R. Purrello, E. Rizzarelli, G. Tabbì, J. Chem. Soc. Dalton Trans. (1998) 3851–3857.
[81] R.P. Bonomo, G. Impellizzeri, G. Pappalardo, E. Rizzarelli, G. Tabbi, Chem. Eur. J. 6 (2000) 4195–4202.
[82] I. Szilágyi, I. Labádi, K. Hernadi, I. Pálinkó, N.V. Nagy, L. Korecz, A. Rockenbauer, Z. Kele, T. Kiss, J. Inorg. Biochem. 99 (2005) 1619–1629.
[83] P.K. Coughlin, S.J. Lippard, Inorg. Chem. 23 (1984) 1446–1451.
[84] T. Storr, P. Verma, R.C. Pratt, E.C. Wasinger, Y. Shimazaki, T. Daniel, P. Stack, J. Am. Chem. Soc. 130 (2008) 15448–15459.
[85] L. Chiang, K. Herasymchuk, F. Thomas, T. Storr, Inorg. Chem. 54 (2015) 5970–5980.
[86] D.E. Richardson, H. Taube, Inorg. Chem. 20 (1981) 1278–1285.
[87] C.-L. O'Young, J.C. Dewan, H.R. Lilienthal, S.J. Lippard, J. Am. Chem. Soc. 100 (1978) 7291–7300.
[88] T.G. Fawcett, E.E. Bernaducci, K. Krogh-Jesperson, H.J. Schugar, J. Am. Chem. Soc. 102 (1980) 2598–2604.
[89] M.M. Bhadbhade, D. Srinivas, Inorg. Chem. 32 (1993) 5458–5466.
[90] Z. Zhang, X. Li, C. Wang, C. Zhang, P. Liu, T. Fang, Y. Xiong, W. Xu, Dalton Trans. 41 (2012) 1252–1258.
[91] G.A. van Albada, W.J.J. Smeets, A.L. Spek, J. Reedijk, Inorg. Chim. Acta 260 (1997) 151–161.
[92] U. Weser, L.M. Shubotz, J. Mol. Catal. 13 (1981) 249–261.
[93] I. Szilágyi, I. Labádi, K. Hernadi, I. Pálinkó, I. Fekete, L. Korecz, A. Rockenbauer, T. Kiss, New J. Chem. 29 (2005) 740–745.
[94] B. Verdejo, S. Blasco, E. García-España, F. Lloret, P. Gaviña, C. Soriano, S. Tatay, H.R. Jiménez, A. Doménech, J. Latorre, Dalton Trans. (2007) 4726–4737.
[95] R.N. Patel, Spectrochim. Acta A 60 (2004) 2201–2208.
[96] B.H.J. Blelski, G.G. Shiue, S. Bajuk, J. Phys. Chem. 84 (1980) 830–833.
[97] M. Simic, I. Taub, J. Tucci, P. Hurwitz, Biochem. Biophys. Res. Commun. 62 (1975) 161–167.